The Astrophysical Journal, 798:69 (19pp), 2015 January 10 doi:10.1088/0004-637X/798/2/69

PLANET FORMATION IN STELLAR BINARIES. I. PLANETESIMAL DYNAMICS IN MASSIVE PROTOPLANETARY DISKS

Roman R. Rafikov and Kedron Silsbee
Department of Astrophysical Sciences, Princeton University, Ivy Lane, Princeton, NJ 08540, USA; rrr@astro.princeton.edu
Received 2014 May 28; accepted 2014 September 4; published 2014 December 23

ABSTRACT

About 20% of exoplanets discovered by radial velocity surveys reside in stellar binaries. To clarify their origin one has to understand the dynamics of planetesimals in protoplanetary disks within binaries. The standard description, accounting for only gas drag and gravity of the companion star, has been challenged recently, as the gravity of the protoplanetary disk was shown to play a crucial role in planetesimal dynamics. An added complication is the tendency of protoplanetary disks in binaries to become eccentric, giving rise to additional excitation of planetesimal eccentricity. Here, for the first time, we analytically explore the secular dynamics of planetesimals in binaries such as α Cen and γ Cep under the combined action of (1) gravity of the eccentric protoplanetary disk, (2) perturbations due to the (coplanar) eccentric companion, and (3) gas drag. We derive explicit solutions for the behavior of planetesimal eccentricity $\mathbf{e}_p$ in non-precessing disks (and in precessing disks in certain limits). We obtain the analytical form of the distribution of the relative velocities of planetesimals, which is a key input for understanding their collisional evolution. Disk gravity strongly influences relative velocities and tends to push the sizes of planetesimals colliding with comparable objects at the highest speed to small values, $\sim$1 km. We also find that planetesimals in eccentric protoplanetary disks apsidally aligned with the binary orbit collide at lower relative velocities than in misaligned disks. Our results highlight the decisive role that disk gravity plays in planetesimal dynamics in binaries.

Key words: binaries: close – planetary systems – planets and satellites: formation – protoplanetary disks

1. INTRODUCTION

Results of radial velocity surveys demonstrate that $\sim$20% of exoplanets reside in stellar binaries (Desidera & Barbieri 2007). While most of these binaries have wide separation between stellar components (hundreds of AU), some of them are systems with relatively short binary periods of $\sim$100 yr. One of the best examples of such a binary is γ Cephei (Hatzes et al. 2003), which consists of two stars with masses of $M_p = 1.6\,M_\odot$ and $M_s = 0.41\,M_\odot$ with a semi-major axis of $a_b = 19$ AU (orbital period $P_b = 58$ yr) and an eccentricity of $e_b = 0.41$. The planet with the projected mass $M_{\rm pl}\sin i = 1.6\,M_J$ is in orbit around the primary with a semi-major axis of $a_{\rm pl} \approx 2$ AU. Several more planetary systems within tight ($a_b \approx 20$ AU) binaries are known at present (Chauvin et al. 2011), including the terrestrial planet around our stellar neighbor α Cen (Dumusque et al. 2012; see Hatzes 2013).

For a long time, theorists struggled to explain the origin of planets in such S-type (according to Dvorak's 1982 classification) systems. The issue lies in the strong dynamical excitation to which any object in a binary is subjected. Gravitational perturbations due to the eccentric companion are expected to adversely affect planet formation already at the stage of planetesimal growth. As first shown by Heppenheimer (1978), companion perturbations drive planetesimal eccentricities to high values, easily approaching 0.1 at 2 AU from the primary. Planetesimals would then be colliding at relative speeds of a couple km s^{-1}, which is much higher than the escape speed from the surface of even a 100 km object (about 100 m s^{-1}). As a result, collisions should lead to planetesimal destruction rather than growth.

A number of possibilities have been explored to at least alleviate this problem. In particular, Marzari & Scholl (2000) studied the dissipative effects of gas drag as the means of damping the relative velocities of planetesimals. These authors have shown that for a circular disk in secular approximation, gas drag induces an alignment of planetesimal orbits such that the periapses of small objects strongly affected by gas drag tend to cluster around $3\pi/2$ with respect to the binary apsidal line. This was originally thought (Marzari & Scholl 2000; Thébault et al. 2004) to assist planetesimal agglomeration since the relative velocities of colliding bodies are reduced by such orbital phasing. However, it was subsequently recognized (Thébault et al. 2008) that the reduction of the relative velocity caused by apsidal alignment is effective only for planetesimals of similar sizes. Objects of different sizes still collide at high speeds, which complicates their growth.

These studies have generally arrived at the same conclusion—the difficulty of planetesimal accretion—despite the different ways in which the gas disk and its interaction with planetesimals was treated. While the early calculations (Thébault et al. 2004, 2006, 2008, 2009; Thébault 2011) typically assumed disk properties to be described by some (semi-)analytic axisymmetric models, several recent studies followed the properties and evolution of gas disks in binaries using direct hydrodynamical simulations (Paardekooper et al. 2008; Kley et al. 2008; Marzari et al. 2009a, 2012; Regály et al. 2011; Müller & Kley 2012; Picogna & Marzari 2013). One of the most important aspects of disk physics that the latter captures is the development of non-axisymmetry in the surface density distribution of the gaseous disk. This non-axisymmetry emerges under the gravitational perturbation of the binary companion, predominantly in the form of non-zero eccentricity of the fluid trajectories (Marzari et al. 2012). Another phenomenon is the disk precession, which sometimes develops in simulations and has a subsequent effect on planetesimal dynamics.

An entirely different way of lowering planetesimal eccentricities in binaries has been pursued by Rafikov (2013, hereafter R13), who demonstrated that planetesimal eccentricities can be considerably lower than previously thought by properly accounting for the gravity of a massive axisymmetric gaseous disk in which planetesimals form. The non-Keplerian potential of the disk drives rapid precession of planetesimal orbits, suppressing the companion's driving of their eccentricity.

Note that massive protoplanetary disks must have been quite natural in γ Cep-like systems since all of the known systems (with the exception of α Cen) harbor Jupiter-like planets with $M_{\rm pl}\sin i = (1.6\text{–}4)\,M_J$ (Chauvin et al. 2011). It is natural to expect the parent disk mass to exceed the planet mass by at least a factor of several (this number is very uncertain but is believed to be $\sim$10 for the Minimum Mass Solar Nebula), which does not make an assumption of a (0.01–0.1) $M_\odot$ disk unreasonable despite the fact that sub-millimeter surveys find very low fluxes of thermal dust emission in young binaries with semi-major axes of several tens of AU (Harris et al. 2012).

As discussed above, the assumption of a purely axisymmetric disk may be too simplistic since simulations indicate that protoplanetary disks in binaries often develop significant eccentricities. To that effect, Silsbee & Rafikov (2015, hereafter SR15) presented the first investigation of the secular excitation of planetesimal eccentricities by the simultaneous action of the gravitational perturbations due to both the eccentric gaseous disk and the companion star. They showed that the non-axisymmetric gravitational field of such a disk excites planetesimal eccentricity (in addition to the excitation produced by the companion) and usually does not allow it to drop below the disk eccentricity, which may be rather high as suggested by some simulations (Okazaki et al. 2002; Paardekooper et al. 2008; Kley & Nelson 2008). This would again suppress planetesimal growth. On the other hand, SR15 outlined several ways in which this issue can be alleviated, for example, if the gaseous disk is precessing rapidly or if its own self-gravity is capable of reducing disk eccentricity to low levels. At the same time, SR15 did not include gas drag in their calculations, eliminating the possibility of planetesimal apsidal alignment and their eccentricity damping by drag.

Our current work builds upon the results of previous studies by exploring planetesimal dynamics in disks coplanar with the binary under the combined effects of (1) gravitational perturbations due to the eccentric gaseous disk in which planetesimals are embedded, (2) the gravity of the eccentric companion, and (3) gas drag. While we do not model disks in binaries using hydrodynamical simulations, we still capture their main features, namely their non-axisymmetry and the possibility of precession. Our results are then used in a companion paper (Rafikov & Silsbee 2015, hereafter Paper II) to explore the details of planet formation in binaries.

We thereby extend the existing semi-analytical studies in which only gas drag (and not disk gravity) was accounted for (Thébault et al. 2004, 2006, 2008, 2009; Leiva et al. 2013). We also go beyond the works of R13 and SR15 in which gas drag was neglected and only the gravitational effects of the gaseous disk and binary companion were considered. In addition, we extend the study of Beaugé et al. (2010) devoted to exploring planetesimal dynamics in eccentric, precessing disks by accounting for the gravitational potential of such a disk.

This paper is structured as follows. We discuss our general setup in Section 2 and then derive equations for the evolution of orbital elements of planetesimals in eccentric disks in Section 3. A prescription for the gas-drag-induced eccentricity evolution is described in Section 4. Solutions to the equations of planetesimal dynamics in non-precessing and precessing disks are presented in Sections 5 and 6 (as well as Appendices B and C) correspondingly. The diversity of planetesimal dynamical behavior is discussed in Section 7. We derive the relative velocity distribution of objects of different sizes in Section 8. We provide an extensive discussion of our dynamical results and their applications in Section 10. We compare different approximations for treating planetesimal dynamics in Section 10.1, briefly discuss limitations of this work in Section 10.2, and summarize our main conclusions in Section 11. Finally, some of our analytical derivations use the local approximation for treating elliptical motion, which is reviewed in Appendix A.

2. PROBLEM SETUP

Our general setup is similar to that explored in SR15. We consider an elliptical disk around a primary star in a binary with semi-major axis a_b, eccentricity e_b, and component masses M_p (primary) and M_s (secondary). We define $\mu \equiv M_s/(M_p + M_s)$ and $\nu \equiv M_s/M_p$. Binary, disk, and planetesimal orbits within it are assumed to be coplanar. This distinguishes our work from many other studies focused on the effects of Lidov–Kozai oscillations (Lidov 1962; Kozai 1962) on planetesimal dynamics in systems with inclined companions (Marzari et al. 2009a; Batygin et al. 2011; Zhao et al. 2012).

Non-axisymmetric disk structure is described via the non-zero disk eccentricity, which is a viable approximation given that simulations tend to show the prevalence of the $m = 1$ azimuthal harmonic of the disk shape distortion (Marzari et al. 2012). Fluid elements in a disk follow elliptical trajectories with an eccentricity $e_g(a_d)$ that is a function of the semi-major axis a_d of a particular ellipse. All of them have the primary star of the binary as a focus. For simplicity, we assume all fluid elliptical trajectories have aligned apsidal lines, uniquely determining disk orientation via a single parameter ϖ_d—the angle between the disk and binary apsidal lines. The latter is assumed to be fixed in space as the precession of the binary under the gravity of the disk is slower than all other processes. The assumption of apsidal alignment does not affect the qualitative features of planetesimal dynamics and can be easily relaxed using the results of Statler (2001).

Because gas moves on ellipses, its surface density generally varies along the trajectory (Statler 2001; Ogilvie 2001). To obtain the gas surface density $\Sigma(r_d, \phi_d)$ at a point in a disk with polar coordinates (r_d, ϕ_d), we specify the gas surface density at periastron for each elliptical trajectory $\Sigma_p(a_d)$ as a function of the semi-major axis of the corresponding ellipse a_d. SR15 show how this and the knowledge of $e_g(a_d)$ can be used to derive $\Sigma(r_d, \phi_d)$ everywhere in the disk. In this work, following SR15, we assume a simple power-law dependence for both e_g and Σ_p:

$$\Sigma_p(a_d) = \Sigma_0 \left(\frac{a_{\rm out}}{a_d}\right)^p, \quad e_g(a_d) = e_0 \left(\frac{a_{\rm out}}{a_d}\right)^q, \qquad (1)$$

where $a_{\rm out}$ is the semi-major axis of the outermost elliptical trajectory of the disk, and Σ_0 and e_0 are the values of Σ_p and e_g at $a_{\rm out}$. The gravity of the companion truncates the disk at this outer radius $a_{\rm out}$, which for eccentric binaries with $e_b = 0.4$ is about $(0.2\text{–}0.3)a_b$ (Artymowicz & Lubow 1994; Regály et al. 2011). Unless stated otherwise, we will be using $a_{\rm out} = 5$ AU in this work.

In all calculations of this paper we will be using a disk model with $p = 1$ and $q = -1$. Some motivation for singling out these particular values of p and q for circumstellar disks in binaries has been provided in R13 and SR15.

The total disk mass $M_d \approx 2\pi \int_{a_{\rm in}}^{a_{\rm out}} \Sigma_p(a_d) a_d da_d$ enclosed within $a_{\rm out}$ can be used to express Σ_p as

$$\Sigma_p(a_d) = \frac{2-p}{2\pi}\frac{M_d}{a_{\rm out}^2}\left(\frac{a_{\rm out}}{a_d}\right)^p \approx 3\times 10^3 {\rm g\ cm^{-2}} M_{d,-2} a_{\rm out,5}^{-1} a_{d,1}^{-1} \quad (2)$$

(the numerical estimate is for $p = 1$), where $M_{d,-2} \equiv M_d/(10^{-2}\,M_\odot)$, $a_{\rm out,5} \equiv a_{\rm out}/(5\,{\rm AU})$ and $a_{d,1} \equiv a_d/{\rm AU}$. In Equation (2) we neglected disk ellipticity and assumed $p < 2$, so that most of the disk mass is concentrated in its outer part.

3. BASIC EQUATIONS

We are interested in the dynamics of planetesimals orbiting the primary within the disk and coplanar to it. We characterize their orbits with the semi-major axis a_p, the eccentricity e_p, and the apsidal angle (with regard to the binary apsidal line) ϖ_p. The orbital evolution of planetesimals is treated in a secular approximation, i.e., neglecting short-term gravitational perturbations (Murray & Dermott 1999). We also assume $e_p \ll 1$ as well as $e_g \ll 1$ and introduce, for convenience, the planetesimal eccentricity vector $\mathbf{e}_p = (k_p, h_p) = e_p(\cos\varpi_p, \sin\varpi_p)$.

In this work, we fully account for gravitational perturbations due to both the binary companion and the eccentric disk using the approach advanced in SR15. For the disk properties described by Equation (1), SR15 calculated an analytic expression for the planetesimal disturbing function accounting for the gravity of both the disk and the secondary. They then derived a set of Lagrange equations (see their Equations (16) and (17)) describing the evolution of $\mathbf{e}_p$ under the influence of gravitational forces alone.

In addition, we take into account the effects of gas drag on the secular evolution of planetesimal eccentricity. Drag-induced dissipation also results in non-conservation of energy and evolution of a_p. However, to zeroth order, we can neglect this since the radial inspiral of planetesimals usually occurs on much longer timescales than their eccentricity evolution (Adachi et al. 1976). As a result, we can concentrate on the behavior of $\mathbf{e}_p$ at fixed a_p and determine the relative velocities of planetesimals and their collisional outcomes.

Gas drag introduces additional terms in the eccentricity evolution equations of SR15, which we re-write in the following form:

$$\frac{dh_p}{dt} = Ak_p + B_b + B_d\cos\varpi_d(t) + \dot{h}_p^{\rm drag}, \quad (3)$$

$$\frac{dk_p}{dt} = -Ah_p - B_d\sin\varpi_d(t) + \dot{k}_p^{\rm drag}. \quad (4)$$

Here $A = A_b + A_d$ is the planetesimal precession rate. It is contributed both by the gravity of the secondary (A_b) and the disk (A_d), with

$$A_b = \frac{\nu}{4} n_p \alpha_b^2 b_{3/2}^{(1)}(\alpha_b) \approx \frac{3}{4} n_p \nu \left(\frac{a_p}{a_b}\right)^3 \approx 5.9\times 10^{-4}{\rm yr^{-1}}\nu\frac{M_{p,1}^{1/2}}{a_{b,20}} a_{p,1}^{3/2}, \quad (5)$$

where $n_p = (GM_p/a_p^3)^{1/2}$ is the planetesimal mean rate, $M_{p,1} \equiv M_p/M_\odot$, $a_{p,1} \equiv a_p/{\rm AU}$, $a_{b,20} \equiv a_b/(20\,{\rm AU})$, $b_s^{(j)}(\alpha)$ is the standard Laplace coefficient (Murray & Dermott 1999), $\alpha_b \equiv a_p/a_b$ and the approximation in Equation (5) works for $\alpha_b \ll 1$. The disk contribution is

$$A_d = 2\pi\frac{G\Sigma_p(a_p)}{a_p n_p}\psi_1 = (2-p)\psi_1 n_p \frac{M_d}{M_p}\left(\frac{a_p}{a_{\rm out}}\right)^{2-p} \approx -6.3\times 10^{-3}{\rm yr^{-1}} a_{p,1}^{-1/2}\frac{M_{d,-2}}{M_{p,1}^{1/2} a_{\rm out,5}}, \quad (6)$$

where the numerical estimate is for $p = 1$ so that $\psi_1 = -0.5$ (SR15). Dimensionless coefficients of order unity ψ_1 and ψ_2 (see Equation (8)) have been calculated in SR15 and are functions of the disk model and the distance of the planetesimal orbit from the disk edges. One can see that for reasonable assumptions about the disk mass ($M_d \sim 10^{-2}\,M_\odot$), the planetesimal precession rate at 1 AU is dominated by the disk gravity.

Eccentricity excitation by the binary (B_b) and the disk (B_d) is described by

$$B_b = -\frac{\nu}{4} n_p \alpha_b^2 b_{3/2}^{(2)}(\alpha_b) e_b \approx -\frac{15}{16} n_p \nu \left(\frac{a_p}{a_b}\right)^4 e_b, \quad (7)$$

$$B_d = \pi\frac{G\Sigma_p(a_p)}{a_p n_p} e_d(a_p)\psi_2, \quad (8)$$

$$= \frac{2-p}{2}\psi_2 e_g(a_p) n_p \frac{M_d}{M_p}\left(\frac{a_p}{a_{\rm out}}\right)^{2-p}, \quad (9)$$

with the latter explicitly depending on the local value of the disk eccentricity $e_g(a_p)$.

Note that ϖ_d in Equations (3) and (4) is not necessarily constant—it can be an explicit function of time, allowing one to treat the case of a precessing disk.

The terms $\dot{h}_p^{\rm drag}$ and $\dot{k}_p^{\rm drag}$, absent in the original version of Equations (3) and (4) in SR15, represent the effect of gas drag on the eccentricity evolution; they are derived in Section 4. The main goal of this work is to see how their introduction affects planetesimal dynamics.

4. DRAG FORCE CALCULATION

Next we derive the expressions for the drag-induced eccentricity evolution terms $\dot{h}_p^{\rm drag}$ and $\dot{k}_p^{\rm drag}$ applicable to the case of an eccentric disk.

Because of our assumption of small eccentricities for both gas and planetesimals, it is reasonable to employ the local (or guiding center) approximation. This approach is often used in studies of planetesimal and galactic dynamics (Binney & Tremaine 2008) and forms a basis of the so-called Hill approximation (Hénon & Petit 1986; Hasegawa & Nakazawa 1990). Local approximation considers planetesimal motion in a local Cartesian $x-y$ reference system aligned with the radial and azimuthal directions, respectively. The main features of this approximation are reviewed in Appendix A. In particular, Equations (A8) describe how k_p and h_p evolve under the effect of external force $\mathbf{F}$.

In our case, **F** is the drag force arising because of the motion of planetesimals with respect to gas. Adachi et al. (1976) gives the following expression for quadratic drag force appropriate for rapidly moving objects with sizes larger than the mean free path of gas molecules:

$$\mathbf{F} = -\frac{C_D}{2}\pi d_p^2 \rho_g v_r \mathbf{v}_r, \quad (10)$$

where C_D is a constant drag coefficient taken to be 0.5 throughout this paper, d_p is the particle size, and ρ_g is the gas density. The relative particle–gas velocity $\mathbf{v}_r$ is given by Equations (A5)–(A7) with relative particle–gas eccentricity components

$$h_r = h_p - h_g, \quad k_r = k_p - k_g, \quad (11)$$

and $\mathbf{e}_g = (k_g, h_g) = e_g(\cos\varpi_d, \sin\varpi_g)$ being the local value of the gas eccentricity vector. Using these expressions, we obtain the force components F_x and F_y:

$$F_x = -\frac{3C_D}{8} m_p D v_r^a (k_r \sin n_p t - h_r \cos n_p t), \quad (12)$$

$$F_y = -\frac{3C_D}{16} m_p D v_r^a (k_r \cos n_p t + h_r \sin n_p t), \quad (13)$$

where m_p is the planetesimal mass, and the relative velocity v_r^a is given by Equation (A7). The prefactor D is given by

$$D = n_p \frac{\Sigma_g}{\rho_p d_p}\frac{r}{h}, \quad (14)$$

with ρ_p being the particle bulk density and $h = c_s/n_p$ being the disk scale height ($c_s = (kT_g/\mu)^{1/2}$).

Now we plug the expressions for F_x, F_y into the first two Equations (A8) and then average them in time t over the planetesimal orbital period (this is the secular, i.e., time-averaged approximation). One can easily see that to get the result to lowest-order in e_r we do not need to keep the terms $O(e_r, e_d, e_p)$ in the expression for ρ_g. As a result, we find

$$\dot{k}_p^{\rm drag} = -\frac{3C_D}{4\pi}\mathrm{E}\left(\frac{\sqrt{3}}{2}\right) D k_r e_r, \quad (15)$$

$$\dot{h}_p^{\rm drag} = -\frac{3C_D}{4\pi}\mathrm{E}\left(\frac{\sqrt{3}}{2}\right) D h_r e_r, \quad (16)$$

where $E(\sqrt{3}/2) \approx 1.211$ is a complete elliptic integral, and $e_r^2 = k_r^2 + h_r^2$.

We can rewrite Equations (15) and (16) in the following form:

$$\dot{k}_p^{\rm drag} = -\frac{k_p - k_g}{\tau_d}, \quad \dot{h}_p^{\rm drag} = -\frac{h_p - h_g}{\tau_d}, \quad (17)$$

where the eccentricity damping time

$$\tau_d = \frac{4\pi}{3C_D \mathrm{E}\left(\sqrt{3}/2\right)} D^{-1} e_r^{-1}$$

$$\approx 600\ \mathrm{yr}\ C_D^{-1} \frac{a_{\rm out,5} a_{p,1}}{M_{p,1}^{1/2} M_{d,-2}} \frac{h/r}{0.1}\frac{10^{-2}}{e_r} d_{p,1}. \quad (18)$$

Here $d_{p,1} \equiv d_p/(1\,\mathrm{km})$ and numerical estimate is for $p = 1$ and $\rho_p = 3\,\mathrm{g\,cm^{-3}}$; in the case of quadratic drag law (10) τ_d depends on k_p and h_p through e_r; see Equations (11).

5. ECCENTRICITY EVOLUTION

Results of Section 4 allow us to understand the behavior of $\mathbf{e}_p$. For simplicity, we start by considering the case of a non-precessing disk, i.e., ϖ_d =const. Even in this case Equations (3) and (4) with the quadratic drag terms (15) and (16) cannot generally be solved analytically because of the τ_d dependence on e_r.

However, it can be easily shown that solutions of these equations inevitably converge to a steady-state form—the free eccentricity, which depends on initial conditions (R13; SR15), damps out and $\mathbf{e}_p$ converges to the forced eccentricity vector (Beaugé et al 2010). This is illustrated in Figure 1 where we solve evolution equations numerically. It is clear that starting with arbitrary initial conditions and after initial (sometimes oscillatory) evolution, k_p and h_p do converge to the same steady state values (depending only on the disk parameters and planetesimal size), which are given by Equations (22) and (23) derived below. This point is additionally illustrated in Figure 2(a) where we plot the trajectory of $\mathbf{e}_p$ as it evolves in h_r–k_r coordinates. There one can clearly see $\mathbf{e}_p$ converging to a fixed point solution, in an oscillatory fashion for large planetesimals, and exponentially for small objects, which rapidly couple to the gas disk.

Damping of the memory of initial conditions can also be demonstrated by solving Equations (3) and (4) analytically in the simplified but qualitatively similar case of a linear drag law, when τ_d is independent of h_p and k_p. Such a solution is presented in Appendix B for the general case of a precessing gaseous disk. The non-precessing disk solution is obtained by setting $\dot{\varpi}_d = 0$. This clearly demonstrates the convergence of $\mathbf{e}_p$ to a time-independent, forced value.

SR15 have demonstrated that in the absence gas drag, under the action of only the gravity of the disk and the companion star, the steady state (forced) eccentricity is given by

$$\mathbf{e}_p^{\rm n/drag} = \begin{Bmatrix} k_p^{\rm n/drag} \\ h_p^{\rm n/drag} \end{Bmatrix} = \mathbf{e}_b + \mathbf{e}_d, \quad (19)$$

$$\mathbf{e}_b = \begin{Bmatrix} k_b \\ h_b \end{Bmatrix} = -\frac{B_b}{A}\begin{Bmatrix} 1 \\ 0 \end{Bmatrix}, \quad (20)$$

$$\mathbf{e}_d = \begin{Bmatrix} k_d \\ h_d \end{Bmatrix} = -\frac{B_d}{A}\begin{Bmatrix} \cos\varpi_d \\ \sin\varpi_d \end{Bmatrix}, \quad (21)$$

where $\mathbf{e}_b$ and $\mathbf{e}_d$ are forced eccentricity vectors due to the secondary and disk gravity, respectively. Note that the accuracy of the analytical expression (20) for the binary contribution is known to worsen (beyond the ~10% level) when $a_p/a_b \gtrsim 0.1$ (Thébault et al. 2006; Barnes & Greenberg 2006). More refined calculations of $\mathbf{e}_b$ are possible (Veras & Armitage 2007; Giuppone et al. 2011) but for the purposes of this work it is sufficient to use Equation (20).

With the gas drag included, the behavior of $\mathbf{e}_p$ changes. To determine the steady-state values of k_p and h_p and analyze their properties, we use the prescription (17), set to zero time derivatives in the left-hand sides of Equations (3) and (4) and solve the resulting algebraic system with respect to h_p and k_p. We find as a result

$$k_p = k_b + k_d + \frac{(k_g - k_b - k_d) - (h_g - h_d)(A\tau_d)}{1 + (A\tau_d)^2}, \quad (22)$$

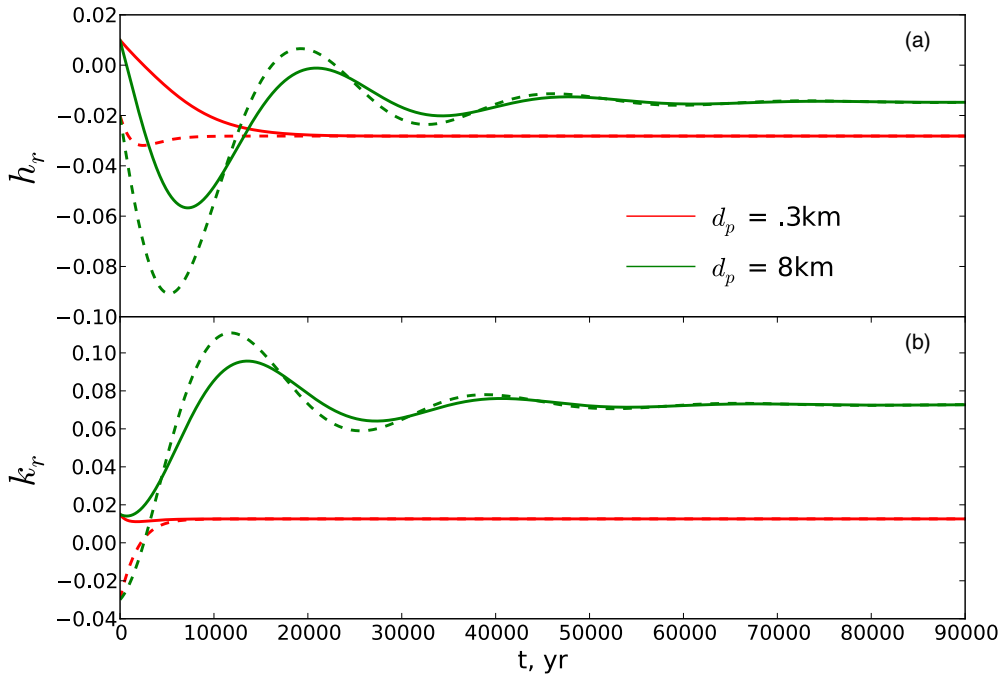

Figure 1. Time evolution of the components of the relative eccentricity vector $\mathbf{e}_r = (k_r, h_r) = \mathbf{e}_p - \mathbf{e}_g$ for planetesimals of two different sizes—$d_p = 0.3$ km (red) and 8 km (green) starting with two different sets of initial conditions—$\mathbf{e}_r = (0.015, 0.01)$ (solid) and $\mathbf{e}_r = (-0.03, -0.02)$ (dashed). Calculations are carried out for the parameters of the γ Cep system at 2 AU in a 0.001 $M_\odot$ disk aligned with the binary; disk eccentricity at its outer edge $a_{\rm out} = 5$ AU is $e_0 = 0.05$, and $p = 1$, $q = -1$ (see Equation (1)). After the short initial transient k_r and h_r converge to the forced values given by Equations (22) and (23).

$$h_p = h_d + \frac{(h_g - h_d) + (k_g - k_b - k_d)(A\tau_d)}{1 + (A\tau_d)^2}, \tag{23}$$

where k_b, k_d, h_b, h_d are defined in Equations (20) and (21). These asymptotic results are valid even if τ_d is a function of e_r —in that case they simply represent two implicit relations for h_p and k_p.

Solutions (22) and (23) can be re-written in vectorial form as

$$\mathbf{e}_p = \begin{Bmatrix} k_p \\ h_p \end{Bmatrix} = \mathbf{e}_{f,b} + \mathbf{e}_{f,d}, \tag{24}$$

$$\mathbf{e}_{f,b} = k_b \frac{(A\tau_d)}{1 + (A\tau_d)^2} \begin{Bmatrix} (A\tau_d) \\ -1 \end{Bmatrix}, \tag{25}$$

$$\mathbf{e}_{f,d} = \left[\frac{e_g^2 + \tau_d^2 B_d^2}{1 + (A\tau_d)^2} \right]^{1/2} \begin{Bmatrix} \cos(\varpi_d + \phi) \\ \sin(\varpi_d + \phi) \end{Bmatrix}, \tag{26}$$

where the phase shift ϕ is given by

$$\cos\phi = \frac{e_g - AB_d\tau_d^2}{\left(e_g^2 + \tau_d^2 B_d^2\right)^{1/2} \left[1 + (A\tau_d)^2\right]^{1/2}}. \tag{27}$$

In the limit of vanishing drag, $A\tau_d \to \infty$, one finds $\phi \to \pi$ and the solution (24)–(26) reduces to the non-drag result with no free eccentricity (19)–(21); see SR15.

In the limit of strong drag ($A\tau_d \to 0$) in a circular disk (i.e., $e_g = 0$) and no disk gravity (i.e., $A_d = B_d = 0$) one finds $h_p/k_p \to -\infty$. This means that in this case planetesimal apsidal lines cluster around $\varpi_p = 3\pi/2$, in agreement with Marzari & Scholl (2000). Also, $|\mathbf{e}_p| \to B_b\tau_d$ directly depends on planetesimal size, which implies that in this limit, planetesimals of different sizes collide with non-zero speeds even despite their apsidal alignment (Thébault et al. 2008).

Expressions (24)–(26) clearly show that $\mathbf{e}_p$ can be split into two distinct components: a contribution $\mathbf{e}_{f,b}$ due to the gravity of the binary and a contribution $\mathbf{e}_{f,b}$ related to both the gravitational and gas drag effects of the disk. It is also clear that after reaching steady state, planetesimal orbits are generally aligned with neither the disk ($\varpi_p \neq \varpi_d$) nor the binary ($\varpi_p \neq 0$).

5.1. Relative Particle–Gas Eccentricity

In the case of quadratic drag (10), we can further analyze eccentricity behavior. Using Equations (22) and (23) we express relative particle–gas eccentricity as

$$e_r = |\mathbf{e}_p - \mathbf{e}_g| = e_c \frac{(A\tau_d)}{\sqrt{1 + (A\tau_d)^2}}, \tag{28}$$

where we introduced a characteristic eccentricity $e_c = |\mathbf{e}_p^{\rm n/drag} - \mathbf{e}_g|$ given by

$$\begin{aligned} e_c &\equiv \left[(h_g - h_d)^2 + (k_g - k_b - k_d)^2\right]^{1/2} \\ &= \frac{\left[(Ae_g + B_d)^2 + B_b^2 + 2\cos\varpi_d B_b (Ae_g + B_d)\right]^{1/2}}{|A|}. \end{aligned} \tag{29}$$

Plugging this expression for e_r into Equation (18), one obtains the following bi-quadratic equation for $(A\tau_d)$:

$$(A\tau_d)^4 = \left(\frac{d_p}{d_c}\right)^2 \left[(A\tau_d)^2 + 1\right], \tag{30}$$

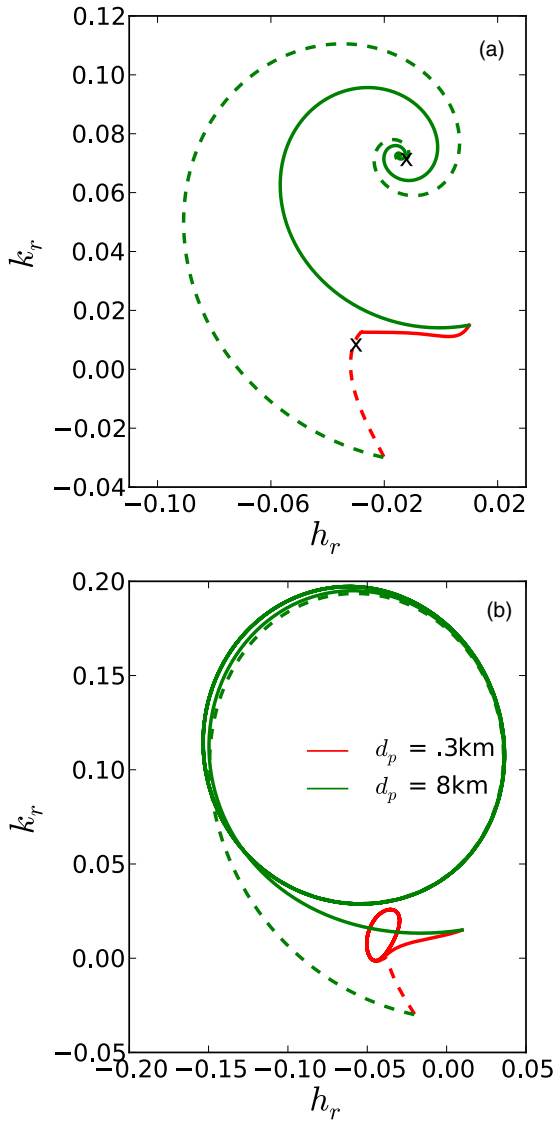

Figure 2. (a) Planetesimal eccentricity evolution trajectories in $k_r - h_r$ space in a non-precessing, aligned ($\varpi_d = 0$) disk for the four cases shown in Figure 1. One can see the convergence of trajectories starting at different $\mathbf{e}_p$ to fixed point solutions (indicated by crosses), which depend on planetesimal radius d_p. (b) The same for a disk precessing at a rate of $\dot{\varpi}_d = A$. Evolution trajectories converge to a limit cycle behavior in the precessing disk. See Section 6 for more details. The color and line type scheme is the same for both panels.

where we have introduced a characteristic planetesimal size d_c defined as

$$d_c \equiv \frac{3C_D \mathrm{E}(\sqrt{3}/2)}{4\pi} \frac{n_p}{|A|} \frac{\Sigma_g}{\rho_p} \frac{r}{h} e_c. \tag{31}$$

All our subsequent results can be formulated completely in terms of e_c and d_p/d_c, underscoring the significance of these variables. A detailed discussion of the characteristic values and general behavior of e_c and d_c is provided in Sections 7.1 and 7.3.

Solving Equation (30), one finds

$$|A\tau_d| = \frac{d_p}{d_c} \left[\frac{1}{2} + \sqrt{\frac{1}{4} + \left(\frac{d_c}{d_p}\right)^2} \right]^{1/2}, \tag{32}$$

i.e., that $|A\tau_d|$ is a function of d_r/d_c only.

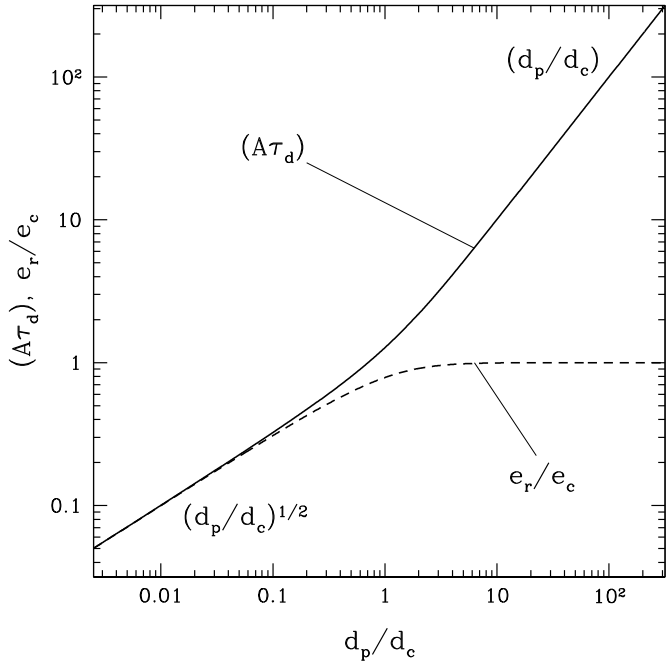

Figure 3. Dependence of e_r/e_c and $|A\tau_d|$ on planetesimal size d_p/d_c, given by Equations (28) and (32), respectively. Asymptotic scalings (34) and (38) are also indicated. For $d_p \sim d_c$ one finds $|A\tau_d| \sim 1$ and $e_r \sim e_c$.

Plugging Equation (32) into Equation (28), one also finds the general expression for the relative particle–gas eccentricity

$$e_r = e_c \frac{d_p}{d_c} \left[\sqrt{\frac{1}{4} + \left(\frac{d_c}{d_p}\right)^2} - \frac{1}{2} \right]^{1/2} \tag{33}$$

valid for arbitrary d_p/d_c.

We illustrate the behaviors of $|A\tau_d|$ and e_r given by Equations (32) and (33) in Figure 3. This reveals the meaning of the characteristic size d_c: objects with $d_p \sim d_c$ have $|A\tau_d| \sim 1$, i.e., their stopping time due to gas drag is comparable to their orbital precession period and their relative eccentricity with respect to gas is $e_r \sim e_c$.

It is instructive to further explore general solutions (32), (33) valid for arbitrary d_p/d_c in the two limits covered next.

5.2. Small Objects, $d_p \lesssim d_c$ — Strong Drag ($|A\tau_d| \lesssim 1$)

In the limit of strong gas drag we expect the damping time τ_d to be very short and $|A\tau_d| \ll 1$, so that the gas-particle velocity differential is rapidly reduced to zero. According to Equation (32), this regime is valid for small objects with $d_p \lesssim d_c$, when

$$|A\tau_d| \approx \left(d_p/d_c\right)^{1/2} \lesssim 1. \tag{34}$$

From Equation (28), the relative particle–gas eccentricity is

$$e_r \approx |A\tau_d|\, e_c \approx e_c \left(d_p/d_c\right)^{1/2} \tag{35}$$

to leading order in $(A\tau_d)$.

Equations (22) and (23) become

$$k_p \to k_g + [(h_d - h_g)(A\tau_d) - (k_g - k_b - k_d)(A\tau_d)^2], \tag{36}$$

$$h_p \to h_g + [(k_g - k_b - k_d)(A\tau_d) + (h_d - h_g)(A\tau_d)^2]. \quad (37)$$

Here brackets encompass the leading order subdominant terms, compared to the zeroth order terms outside brackets.

It is clear from these asymptotic expressions that in the case of strong drag, the eccentricity vector of planetesimals tends toward the eccentricity vector of the gas, $\mathbf{e}_p \to \mathbf{e}_g$. It is only weakly sensitive to gravitational perturbations due to either the companion or the disk. Thus, to leading order, the value of the eccentricity vector is independent of particle size (which enters only through τ_d).

5.3. Big Objects, $d_p \gtrsim d_c$ — Weak Drag ($|A\tau_d| \gtrsim 1$)

In the opposite limit of weak drag or long damping time $|A\tau_d| \gg 1$ valid for large objects with $d_p \gtrsim d_c$, Equation (32) yields

$$(A\tau_d) \approx d_p/d_c \gtrsim 1, \quad (38)$$

while the relative particle–gas eccentricity is

$$e_r \approx e_c; \quad (39)$$

see Equation (28). Thus, in the weak drag regime, e_r saturates at the value independent of the size of the object.

Equations (22) and (23) reduce in this limit to

$$k_p \to k_b + k_d + [(h_d - h_g)(A\tau_d)^{-1} + (k_g - k_b - k_d)(A\tau_d)^{-2}], \quad (40)$$

$$h_p \to h_g + [(k_g - k_b - k_d)(A\tau_d)^{-1} - (h_d - h_g)(A\tau_d)^{-2}]. \quad (41)$$

Again, terms in brackets are subdominant compared to the leading terms (outside brackets).

This solution shows that in the limit of weak drag $\mathbf{e}_p \to \mathbf{e}_p^{\rm n/drag}$, i.e., the behavior of the particle eccentricity vector is determined predominantly by the gravitational effects of the secondary and the disk. Thus, $\mathbf{e}_p$ is again almost independent of the particle size.

6. PRECESSING DISKS

So far we have assumed the orientation of the disk to be fixed in the binary frame. However, some simulations find disks in binaries to precess (e.g., Marzari et al 2009b; Müller & Kley 2012). We now study how planetesimal dynamics change in the case of a disk uniformly precessing at a constant rate of $\dot{\varpi}_d$. Figure 2(b) displays the evolution of $\mathbf{e}_p$ for the same parameters as in panel (a) of that figure, but in a disk precessing at the rate $\dot{\varpi}_d = A$. One can see that the main difference compared to the non-precessing case is that in the long run $\mathbf{e}_p$ converged to limit cycle behavior (Beaugé et al. 2010) rather than to a fixed point, as in panel (a). The sizes and shapes of the asymptotic limit cycles depend on both the planetesimal size d_p and the disk precession rate $\dot{\varpi}_d$, as discussed in detail in Appendix C and shown in Figure 9. This certainly complicates planetesimal dynamics.

To gain additional insights, in Appendix B, we derive a full time-dependent solution for $\mathbf{e}_p$ in a precessing disk for the case of linear gas drag, when τ_d is independent of the relative particle–gas eccentricity e_r. This solution fully accounts for the gravitational and gas drag effects of the precessing disk as well as for the gravity of the binary companion.

We use this solution as a basis for understanding planetesimal dynamics in a precessing disk in the more complicated but realistic case of quadratic gas drag. This regime, which does not admit a general analytical solution even for the long-term behavior, is explored in Appendix C. There we show that planetesimal dynamics with drag law (10) depend on the relative role played by the binary companion, as described in the next section.

6.1. Strong Binary Perturbation Case

The results in Appendices B and C show that whenever binary gravity dominates $\mathbf{e}_p$ excitation and the condition

$$|(A - \dot{\varpi}_d)e_g + B_d| \lesssim |B_b| \quad (42)$$

is fulfilled, planetesimal dynamics proceed as if the disk were not precessing: neither the gas eccentricity e_g nor the eccentricity driven by disk gravity e_d, Equation (21), is significant compared to the forced eccentricity due to the binary $e_b = B_b/A$ (note that both the binary and disk gravity contribute to A).

In this case, $\mathbf{e}_p$ is close to the relative planetesimal-gas eccentricity $\mathbf{e}_r$ and is approximately constant. As a result, the planetesimal orbit maintains a roughly fixed orientation with respect to the binary orbit and

$$k_p \approx k_b \frac{(A\tau_d)^2}{1 + (A\tau_d)^2}, \quad h_p \approx -k_b \frac{(A\tau_d)}{1 + (A\tau_d)^2}, \quad (43)$$

with k_b defined by Equation (20). Planetesimal orbits are aligned with the binary ($\varpi_p \to 0$) for $|A\tau_d| \to \infty$ (weak drag), but in the case of strong drag, $|A\tau_d| \to 0$, the planetesimal apsidal line points at $\varpi_d = 270^\circ$, which agrees with Marzari & Scholl (2000) despite the disk precession.

Interestingly, even though gas eccentricity e_g does not appear in these expressions (and neither does the precession rate $\dot{\varpi}_d$, at the lowest order), the effect of the gas drag is explicitly present via the non-trivial τ_d dependence. Thus, our precessing disk results obtained in the limit (42) apply equally well to planetesimal dynamics in a purely axisymmetric ($e_g = 0$) gaseous disk, extending the results of R13 to the case of non-zero gas drag—note that A in Equations (43) and in the definition of k_b is the full precession rate due to both the binary and the disk.

The value of e_r in the regime (42) is given by Equations (28) and (33) with d_c and $|A\tau_d|$ computed using $e_c \approx e_b = |B_b/A|$ (i.e., Equation (29) in the limit $B_d \to 0$, $e_g \to 0$); see Equations (31) and (32).

6.2. Weak Binary Perturbation Case

In the opposite case of weak driving of $\mathbf{e}_p$ by the binary companion, we combine solutions (C5) and find the relative particle–gas eccentricity to be

$$e_r = \left|e_c^{\rm pr}\right| \frac{|A - \dot{\varpi}_d|\,\tau_d}{\sqrt{1 + (A - \dot{\varpi}_d)^2\,\tau_d^2}}, \quad (44)$$

replacing Equation (28) in the case of the precessing disk. Here we defined the characteristic eccentricity as

$$e_c^{\rm pr} = -\frac{B_d}{A - \dot{\varpi}_d} - e_g, \quad (45)$$

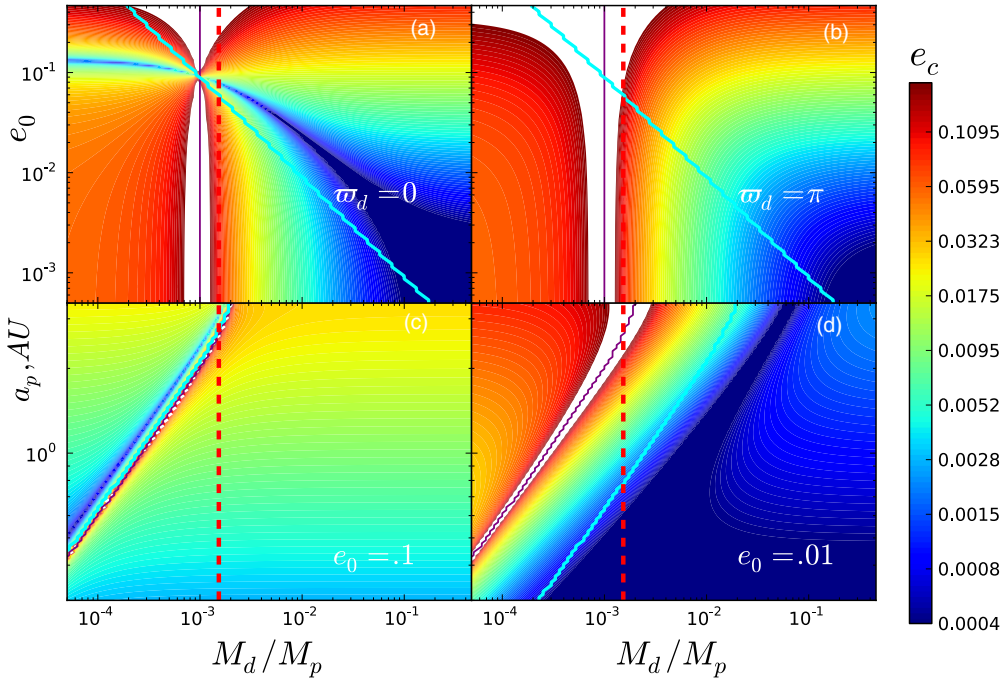

Figure 4. Map of the characteristic eccentricity e_c as a function of e_0 and M_d (upper panels) for two different disk orientations—$\varpi_d = 0$ (a) and (b)—and as a function of a_p and M_d for two values of disk eccentricity e_0 at $a_{\rm out}$ (lower panels). The calculation is done for γ Cep system at $a_p = 2$ AU (the observed semi-major axis of the planet). The dashed red line corresponds to $M_p \sin i$ for the observed planet in the γ Cephei system. The purple line is where $|A_d| = |A_b|$ and the blue line is where $|B_d| = |B_b|$. See the text for details.

which, according to SR15, is the relative particle–gas forced eccentricity in the no drag ($\tau_d \to \infty$) and no binary ($B_b \to 0$) case. As $\dot{\varpi}_d \to 0$, one finds $|e_c^{\rm pr}| \to e_c$ given by Equation (29) with $k_b = h_b = 0$; also, Equation (44) reduces to the non-precessing disk result (28).

Plugging this expression for e_r into Equation (18) one finds

$$|A - \dot{\varpi}_d|\,\tau_d = \frac{d_p}{d_c^{\rm pr}}\left[\frac{1}{2} + \sqrt{\frac{1}{4} + \left(\frac{d_c^{\rm pr}}{d_p}\right)^2}\right]^{1/2}, \qquad (46)$$

with a new characteristic planetesimal size

$$d_c^{\rm pr} \equiv \frac{3C_D {\rm E}(\sqrt{3}/2)}{4\pi}\frac{n_p}{|A - \dot{\varpi}_d|}\frac{\Sigma_g}{\rho_p}\frac{r}{h}\left|e_c^{\rm pr}\right|. \qquad (47)$$

These expressions are different from Equations (31) and (32) in that they use $A - \dot{\varpi}_d$ instead of A and $|e_c^{\rm pr}|$ instead of e_c. It is then clear that whenever a precessing disk dominates the planetesimal dynamics Equation (33) also holds provided that we replace $d_c \to d_c^{\rm pr}$ and $e_c \to |e_c^{\rm pr}|$. The same is true for our asymptotic results on $\mathbf{e}_p$ behavior presented in Sections 5.2 and 5.3 if we also take $k_b \to 0$.

In the limit $\dot{\varpi}_d \to 0$, the value of $\mathbf{e}_f$ reduces to $\mathbf{e}_{f,d}$ given by Equation (26), but when $|\dot{\varpi}_d| \gg |A|$, rapid disk precession suppresses excitation of planetesimal eccentricity by the disk gravity, i.e., the first term in Equation (45).

It is worth noting that the results of Appendix B for the case of linear drag suggest that neglecting binary gravity in the case of a precessing disk might require a condition different from the direct opposite to the constraint (42). Indeed, the asymptotic solution (B5) for the relative eccentricity of planetesimals in the case of weak drag ($\tau_{d,1}, \tau_{d,2} \gg |A - \dot{\varpi}_d|^{-1}$) shows that the term proportional to k_b can be neglected only when

$$|(A - \dot{\varpi}_d)e_g + B_d| \gtrsim |B_b|\left(\frac{A - \dot{\varpi}_d}{A}\right)^2, \qquad (48)$$

which is a more stringent criterion whenever $|\dot{\varpi}_d| \gg |A|$. The same constraint may be needed in the case of quadratic drag. However, in practice, one often finds $|\dot{\varpi}_d| \lesssim |A|$; see Paper II in which case Equation (48) is just the opposite of the condition (42).

7. DIVERSITY OF PLANETESIMAL DYNAMICS

Results of Section 5 demonstrate that the steady state value of the eccentricity vector $\mathbf{e}_p$ is fully determined by just two key parameters—the characteristic eccentricity e_c and the critical planetesimal size d_c; see Equation (33). The eccentricity e_c sets the overall scale of $\mathbf{e}_p$, while d_c is the planetesimal size at which planetesimal coupling to gas changes from weak to strong. We now explore the behavior of these variables as a function of system parameters to elucidate some important features of planetesimal dynamics.

7.1. Behavior of e_c

In Figures 4(a) and (b) we show e_c computed for the γ Cep system at 2 AU—the semi-major axis of its planet—as a function of disk mass M_d and eccentricity e_0, for two disk orientations—aligned ($\varpi_d = 0$) and anti-aligned ($\varpi_d = \pi$) with the apsidal line of the binary.

One can immediately see a feature common to both panels—a narrow valley of high e_c (white because of saturation at high e_c) at almost constant M_d. It appears because at this value of disk mass, $A_d = -A_b$ and $A = 0$, giving rise to a secular resonance. According to Equations (19)–(21) and (29), e_c gets driven to

high values as $A \to 0$. This resonance has been previously discussed in R13 and SR15.

Equations (5) and (6) predict that at a given distance from the primary a_p, this resonance occurs for the disk mass

$$M_{d,A=0} = M_s \frac{3}{4(2-p)|\psi_1|}\left(\frac{a_p}{a_b}\right)^{1+p}\left(\frac{a_{\rm out}}{a_b}\right)^{2-p} \approx 1.5\times 10^{-3}\, M_\odot \frac{M_s}{0.4\, M_\odot}\frac{a_{\rm out,5}}{a_{b,20}^3}a_{p,2}^2, \quad (49)$$

where $a_{\rm out,5} \equiv a_{\rm out}/(5\,{\rm AU})$, $a_{p,2} \equiv a_p/(2\,{\rm AU})$, and $a_{b,20} \equiv a_b/(20\,{\rm AU})$. This estimate agrees with Figures 4(a) and (b) for the γ Cep parameters and a disk with $p = 1$ and $\psi_1(p = 1) = -0.5$ (SR15).

The existence of this resonance is independent of the relative disk–binary orientation because planetesimal precession rates A_b and A_d are determined by the axisymmetric components of the binary and disk gravitational potentials. For this reason, $M_{d,A=0}$ is the same for all disk orientations. To the right of the secular resonance, disk gravity dominates the planetesimal precession rate and suppresses e_c if the disk eccentricity is small (R13).

At high disk eccentricity, typically $e_0 \gtrsim 0.05$, this suppression vanishes because for large $M_d \gtrsim 10^{-3}\, M_\odot$, disk gravity starts to dominate $\mathbf{e}_p$ excitation. This statement is true above the blue line $|B_b| = |B_d|$ in Figures 4(a) and (b) (the origin of the low-e_c band at small M_d and high e_0 in Figure 4(a) is discussed in Section 7.2). Further increase of the disk mass in this region does not affect e_c because the planetesimal dynamics switch to the so-called DD regime (SR15) in which $e_p(a_p) \approx |\psi_2/\psi_1| e_g(a_p)$, independent of M_d. As a result, high e_g leads to high e_p.

In Figures 4(c) and (d) we explore the dependence of e_c on the distance from the binary a_p and M_d for two different values of the disk eccentricity $e_0 = 0.1$ and 0.01. Here we look only at an aligned disk case. Again, an obvious feature of these maps is the secular resonance around the blue dashed curve for $|A_d| = |A_b|$, where e_c is very large and collisional growth is impossible. In Figure 4(d) there is also a "valley" of low e_c to the right of the blue line $|B_b| = |B_d|$, whose origin is discussed in Section 7.2.

These maps make it clear that e_c becomes independent of M_d (at a given separation a_p) when the disk mass becomes large enough. This is a direct consequence of the planetesimal dynamics switching into the DD regime (SR15) when both the eccentricity excitation and apsidal precession of planetesimals are dominated by the disk gravity with a negligible contribution from the binary companion. In the high-M_d regime, e_c decreases as a_p decreases. This is a consequence of our adopted disk model, in which $e_d \propto a_p$ and the fact that $e_c \propto e_d$ in the DD regime.

7.2. Valley of Stability in Aligned Disks

Figures 4(a) and (b) show that irrespective of the disk orientation, e_c is low for high $M_d \gtrsim 10^{-2}\, M_\odot$ and small disk eccentricity, $e_0 \lesssim 10^{-2}$. Outside this corner of phase space, e_c is much higher, which makes planetesimal growth problematic there. At the same time, in the case of an aligned disk ($\varpi_d = 0$), low values of e_c are also possible in a narrow "valley" stretching toward high e_0 and low M_d. Since this feature may have interesting implications for planet formation in binaries (see Paper II for details), we discuss its origin in more detail.

Equation (29) implies that in an aligned disk $h_g = h_d = 0$ so that

$$e_c \approx |k_g - k_d - k_b| = \left|\frac{B_b + B_d + A e_g}{A}\right|. \quad (50)$$

For massive disks, to the right of the vertical $|A_b| = |A_d|$ line in Figure 4(a), one can set $A \approx A_d$ and relate it to B_d via Equations (6) and (8). As a result, Equation (50) becomes

$$e_c \approx \left|\frac{B_b + B_d\left(1 + 2\psi_1\psi_2^{-1}\right)}{A_d}\right|. \quad (51)$$

For the disk model considered here ($p = 1$, $q = -1$), one has $\psi_1 = -0.5$, $\psi_2 = 1.5$ and $1 + 2\psi_1\psi_2^{-1} = 1/3$ so that $e_c \approx |A_d|^{-1}|B_b + B_d/3|$. Also $B_d > 0$ while B_b is always negative; see Equations (7) and (8). Given that $B_d \propto e_0 M_d$ it is then obvious that one can make $e_c \approx 0$ by choosing $e_0 M_d$ such that $|B_b| \approx |B_d|/3$. Thus, in the case of an aligned disk, a "valley" of low e_c is described by the relation $e_0 \propto M_d^{-1}$ as long as $|A_d| \gtrsim |A_b|$ (i.e., for massive disks).

From this discussion we see that $e_c \approx 0$ for values of e_0 and M_d that are close to the curve

$$M_{d,|B_b|=|B_d|} = M_s \frac{15}{8(2-p)|\psi_2|}\frac{e_b}{e_0} \times \left(\frac{a_p}{a_b}\right)^{2+p+q}\left(\frac{a_{\rm out}}{a_b}\right)^{2-p-q} \approx 1.2\times 10^{-3}\, M_\odot \frac{M_s}{0.4\, M_\odot}\frac{e_b}{0.4}\frac{0.1}{e_0}\frac{a_{\rm out,5}^2}{a_{b,20}^4}a_{p,2}^2, \quad (52)$$

on which $|B_b| = |B_d|$; see Equations (7) and (8) in which we took $p = 1$, $q = -1$. This relation is shown by the blue line in Figure 4 and is quite close to the valley of low e_c.

Note that according to Equation (51), the value of e_c can be lowered globally in a massive disk if its structure is such that $1+2\psi_1\psi_2^{-1} = 0$. However, this is not the case for the disk model used in this work.

The situation is different for the low mass, aligned disks to the left of the $|A_d| = |A_b|$ (blue dashed) line in Figure 4(a). Here $A \approx A_b$ and B_b dominates over B_d for low enough M_d at a fixed e_0, which, in the terminology of SR15, corresponds to Case BB of planetesimal excitation. In this regime, Equation (50) shows that

$$e_c \to \left|e_g + \frac{B_b}{A_b}\right| = \left|e_g - \frac{5}{4}\frac{a_p}{a_b}e_b\right| \quad (53)$$

Our adopted radial scaling of e_g in the form Equation (1) with $q = -1$ results in a particular value of

$$e_0\big|_{e_c\to 0} = \frac{5}{4}\frac{a_{\rm out}}{a_b}e_b = 0.125\frac{a_{\rm out}/a_b}{0.25}\frac{e_b}{0.4}, \quad (54)$$

for which $e_c \to 0$. This critical value of e_0 is independent of M_d explaining why the valley of low e_c starts going almost horizontally for $M_d \lesssim M_d\big|_{A=0}$ in Figure 4(a).

Moreover, $e_0|_{e_c\to 0}$ is also independent of a_p, which means that $e_c \to 0$ globally when $e_0 \to e_0|_{e_c\to 0}$ in parts of the disk where $|A_b| \gtrsim |A_d|$ and $|B_b| \gtrsim |B_d|$. This is the reason why in the upper left corner of Figure 4(c) e_c is considerably lower

than in the same region of Figure 4(d), despite e_0 being an order of magnitude higher in the former case. Indeed, according to Equation (54), $e_0 = 0.1$ used in Figure 4(c) is very close to $e_0|_{e_c \to 0}$ for the adopted system parameters. As a result of this coincidence, e_c is strongly suppressed in the BB regime in a rather eccentric ($e_0 = 0.1$) disk.

A narrow region of low e_c stretching along the blue curve $|B_b| = |B_d|$ in Figures 4(c) and (d) is the same valley of stability, but now revealing itself in $M_d - a_p$ coordinates.[1] It may lie inside (for low e_0) as well as outside (for high e_0) of the secular resonance. Note that in Figure 4(c) the $|A_d| = |A_b|$ and $|B_d| = |B_b|$ curves fall almost on top of each other, which is a coincidence caused by our choice of $e_0 = 0.1$ in this case. Because of that, the valley of stability appears as a very narrow band of low e_c just to the left of the $|B_d| = |B_b|$ curve in this panel.

If the disk is not aligned with the binary orbit and ϖ_d is not small, then both h_d and h_g are nonzero and contribute to e_c; see Equation (29). Moreover, for disks that are close to being anti-aligned with the binary, k_b and k_d have the same sign, eliminating the possibility of their mutual cancellation. As a result, the low-e_c valley at high e_0 and low M_d disappears as long as $|\varpi_d - \varpi_b| \gtrsim 10^\circ$.

To summarize, the valley of stability creates favorable conditions for locally lowering planetesimal velocity in aligned disks around some particular locations even in low-mass disks with $M_d \lesssim 10^{-2}\, M_\odot$.

7.3. Behavior of d_c

Next we discuss the behavior of the characteristic size d_c at which planetesimals of similar (but not equal) mass collide at the highest relative velocity $\sim e_c v_K$. Equation (31) shows that for a given value of e_c, critical size d_c scales inversely with the planetesimal precession rate $|A|$. If planetesimal precession is dominated by the potential of the secondary, then $A = A_b$, and one finds

$$d_c = \frac{C_D \mathrm{E}(\sqrt{3}/2)}{\pi \nu} \frac{r}{h} \frac{\Sigma_g}{\rho_p} \left(\frac{a_b}{a_p}\right)^3 e_c$$
$$\approx 30\ \mathrm{km} \frac{C_D}{\nu} \frac{0.1}{h/r} \frac{M_{d,-2} a_{b,20}^3}{a_{\mathrm{out},5}} \frac{e_c}{0.1} a_{p,1}^{-4}, \qquad (55)$$

where the numerical estimate is for a $p = 1$ disk and $\rho_p = 3\ \mathrm{g\,cm^{-3}}$.

In the opposite case, when precession is dominated by the disk gravity and $A = A_d$, one obtains

$$d_c = \frac{3 C_D \mathrm{E}(\sqrt{3}/2)}{8\pi^2 \psi_1} \frac{r}{h} \frac{M_p}{\rho_p a_p^2} e_c$$
$$\approx 1\mathrm{km} \frac{C_D}{\psi_1} \frac{0.1}{h/r} \frac{e_c}{0.1} M_{p,1} a_{p,1}^{-2}, \qquad (56)$$

independent of the disk mass. It is obvious that in the disk-dominated case, d_c is much smaller than in the binary-dominated case for $a_p \lesssim 1\mathrm{AU}$, a fact predicted in R13.

This difference can be easily seen in Figure 8, where the situation depicted in panel (a) corresponds to the DD regime where Equation (56) applies. As a result, the planetesimal size for which the low-e_r "waist" in this figure is narrowest is around 1 km. In constrast, Figure 8(b) shows a situation in which the disk gravity has been turned off, so the dynamics are in the BB regime and Equation (55) applies. Not surprisingly, this pushes the characteristic d_p at the narrowest point of the waist to be about 30 km.

Using this reasoning, one might expect the critical "dangerous" size d_p at which $e_r \sim e_c$ for objects of comparable size to be smaller for more massive disks in which $|A_d| \gg |A_b|$. However, this logic directly applies only if e_c were kept the same. In reality, changing A also directly affects the value of e_c; see Equation (29). Figure 5 shows that in practice, the behavior of d_c largely reflects that of e_c, with all the features of e_c maps (e.g., valleys of low d_c) present in d_c maps as well. In particular, the valley of stability shows up prominently in Figures 5(a) and (d).

The only noticeable difference with Figure 4 is the increase of d_c with decreasing a_p in the high-M_d (DD) regime; see Figures 5(c) and (d), a behavior that is predicted by Equation (56). Also, in agreement with Equation (55), d_c decreases with increasing a_p in the outer disk for small M_d (upper left in Figures 5(c) and (d)) even though e_c varies weakly there. In this region, planetesimal dynamics are determined predominantly by the binary companion (BB regime of SR15) and Equation (55) applies.

8. DISTRIBUTION OF RELATIVE PLANETESIMAL VELOCITIES

Our next step is to study the behavior of the relative approach velocity v_{12} between planetesimals with sizes d_1 and d_2. It is this velocity that determines the outcome of their collision.

We now provide a calculation of the distribution df_{12}/dv_{12} of v_{12} between the two planetesimal populations, one with the eccentricity vector $\mathbf{e}_p(d_1)$ and another with $\mathbf{e}_p(d_2)$. In previous sections, we have shown that after the initial transient period, when the free eccentricity damps out, the value of $\mathbf{e}_p$ becomes time-independent and is uniquely determined by the planetesimal size. Then the only additional orbital parameter that can give rise to the variation of the relative velocity v_{12} is the difference in semi-major axes b_{12} between approaching particles; see Equation (A7) of Appendix A. Using Equations (A4) and (A7), this relation can be written as

$$v_{12} = \Omega a_p \left[e_{12}^2 - \frac{3}{4} \left(\frac{b_{12}}{a_p}\right)^2 \right]^{1/2}, \qquad (57)$$

where a is the mean semi-major axis of both planetesimals, and the condition of close approach $x_{12} = 0$ is used. Note that in this expression we ignored the contribution of particle inclination to the velocity. This is a reasonable assumption since we expect eccentricity excitation in the binary plane to dominate over the out-of-plane excitation.

Ida et al. (1993) consider encounters between the two populations of objects with fixed eccentricity vectors $\mathbf{e}_1 = (k_1, h_1)$ and $\mathbf{e}_2 = (k_2, h_2)$. They derive the following expression for the flux of objects with an eccentricity $\mathbf{e}_2$ approaching a given object with an eccentricity $\mathbf{e}_1$ with random orbital phases, having a separation of their semi-major axes b_{12} in the range $(b_{12}, b_{12}+db_{12})$:

$$dF_{12} = \frac{1}{\pi^2} \frac{\Sigma_2}{a_p m_2 i_{12}} \frac{v_{12} db_{12}}{\left[e_{12}^2 - (b_{12}/a_p)^2\right]^{1/2}}. \qquad (58)$$

[1] Curves of $|A_d| = |A_b|$ and $|B_d| = |B_b|$ run parallel to each other in Figures 4(c) and (d) because $e_d \propto a_p$ in our disk model; see Equations (5) and (8).

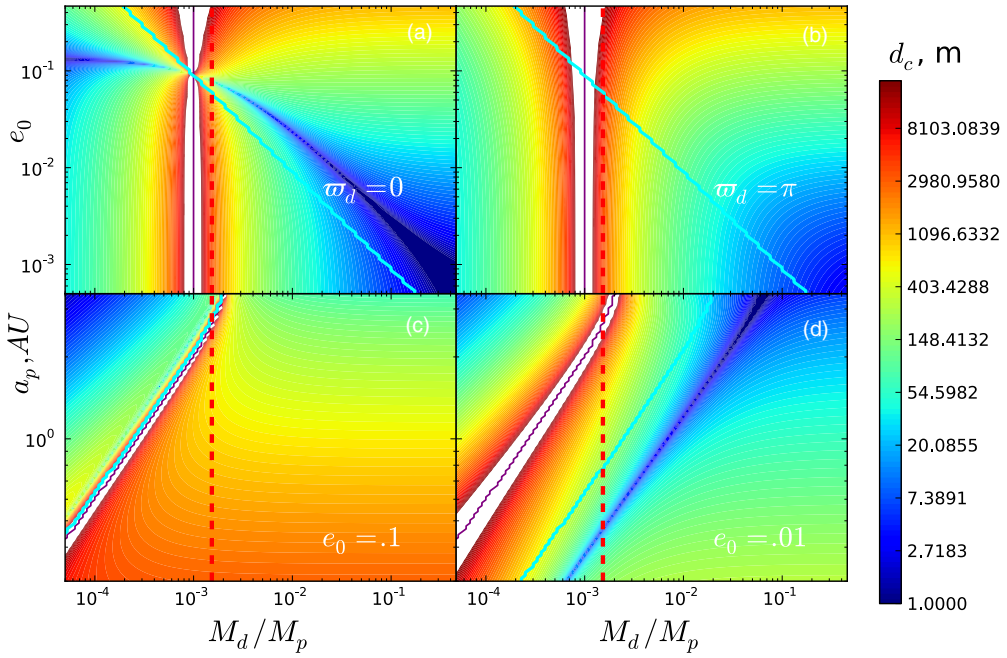

Figure 5. Same as Figure 4 but for the behavior of the characteristic size d_c given by Equation (31).

Here $e_{12} = [(h_1 - h_2)^2 + (k_1 - k_2)^2]^{1/2}$ is the relative eccentricity between the two particle populations, i_{12} is their relative inclination, and Σ_2 is the surface density of objects with eccentricity $\mathbf{e}_2$.

Using Equation (57), we can express db in Equation (58) via dv_{12}, resulting in a differential particle flux per unit v_{12}

$$\frac{dF_{12}}{dv_r} = \frac{4}{3\pi^2}\frac{\Sigma_2 a_p}{m_2 i_{12}}\frac{e_{12}^2 - (3/4)(b_{12}/a_p)^2}{|b_{12}|\left[e_{12}^2 - (b_{12}/a_p)^2\right]^{1/2}}. \quad (59)$$

We now express b_{12} via v_{12} using Equation (57) and introduce

$$v_{\min} = \frac{1}{2}e_{12} n a_p, \quad v_{\max} = e_{12} n a_p. \quad (60)$$

Then it is clear that $v_{\min} < v_{12} < v_{\max}$ and we can re-write (59) as

$$\frac{dF_{12}}{dv_{12}} = \frac{1}{\pi^2}\frac{\Sigma_2}{m_2 i_{12}}\frac{v_{12}^2}{\left[\left(v_{\max}^2 - v_{12}^2\right)\left(v_{12}^2 - v_{\min}^2\right)\right]^{1/2}}. \quad (61)$$

From this we find that the distribution of relative velocities df_{12}/dv_{12} of different planetesimals normalized to unity is given by the following expression:

$$\frac{df_{12}}{dv_{12}} = \frac{v_{\max}^{-1}}{\mathrm{E}(\sqrt{3}/2)}\frac{v_{12}^2}{\left[\left(v_{\max}^2 - v_{12}^2\right)\left(v_{12}^2 - v_{\min}^2\right)\right]^{1/2}}. \quad (62)$$

Particle sizes enter into this expression only through e_{12} via Equations (60).

This distribution of relative velocities is shown in Figure 6. It diverges at both $v = v_{\min}$ and $v = v_{\max}$, but the total particle flux is finite and given by

$$F_{12} = \int_{v_{\min}}^{v_{\max}} \frac{dF_{12}}{dv_{12}} dv_{12} = \frac{\mathrm{E}(\sqrt{3}/2)}{\pi^2}\frac{\Sigma_2 e_{\max}}{m_2 i_{12}}. \quad (63)$$

With the distribution function (61), one finds that the mean relative velocity $\langle v_{12}\rangle \approx 0.81 v_{\max} = 0.81 e_{12} n_p a_p$, while the rms velocity is given by $v_{\rm rms} = \langle v_{12}^2\rangle^{1/2} = 0.828 e_{12} n_p a_p$.

9. RELATIVE VELOCITY BETWEEN PLANETESIMALS

The results of the previous section clearly demonstrate that the relative velocity with which two planetesimals with sizes d_1 and d_2 approach each other prior to collision is determined by their relative eccentricity $e_{12} = |\mathbf{e}_p(d_1) - \mathbf{e}_p(d_2)|$. Using solutions (22) and (23), it is trivial to show that

$$e_{12} = e_c \frac{\left|A\tau_{d,1} - A\tau_{d,2}\right|}{\sqrt{\left(1 + A^2\tau_{d,1}^2\right)\left(1 + A^2\tau_{d,2}^2\right)}}, \quad (64)$$

where $\tau_{d,i} \equiv \tau_d(d_i)$, $i = 1, 2$. According to the results of Section 5, $A\tau_d$ and, subsequently, e_{12}, are functions of (1) the sizes of the colliding planetesimals $d_{1,2}$ and (2) the binary parameters and local disk properties, which set the values of both e_c and d_c; see Equations (29) and (31). We already explored the latter in Section 7 and now we turn our attention to understanding $e_{1,2}(d_1, d_2)$.

In Figure 7 we map out $e_{12}(d_1, d_2)$ (as well as the relative velocity $v_{12} = e_{1,2} v_K$) at the location of the planet $a_p = 2$ AU in the γ Cephei system for different characteristics of the disk, for which a model (1) with $p = 1$, $q = -1$ is adopted. We vary disk mass M_d, eccentricity at its outer edge e_0, and its orientation with respect to the binary orbit ϖ_d, one at a time, keeping other disk parameters fixed. All panels clearly show several key invariant features.

First, there is a critical size of order d_c, around $d_1 = d_2 \sim$ (0.1–1) km, at which maps exhibit a "waist," in which e_{12} is small for collisions of equal size bodies. Second, e_{12} becomes small for encounters between both the small bodies, with $d_1, d_2 \lesssim d_c$, and for large objects with $d_1, d_2 \gtrsim d_c$. Third, e_{12} saturates at a value roughly independent of d_1 or d_2 for collisions of particles with very different sizes, i.e., when $d_1 \lesssim d_c \lesssim d_2$, and vice versa.

These gross features, as well as the variations of the overall velocity scale seen in these maps, are addressed below using the results of Section 5. Given that particles can be in different drag

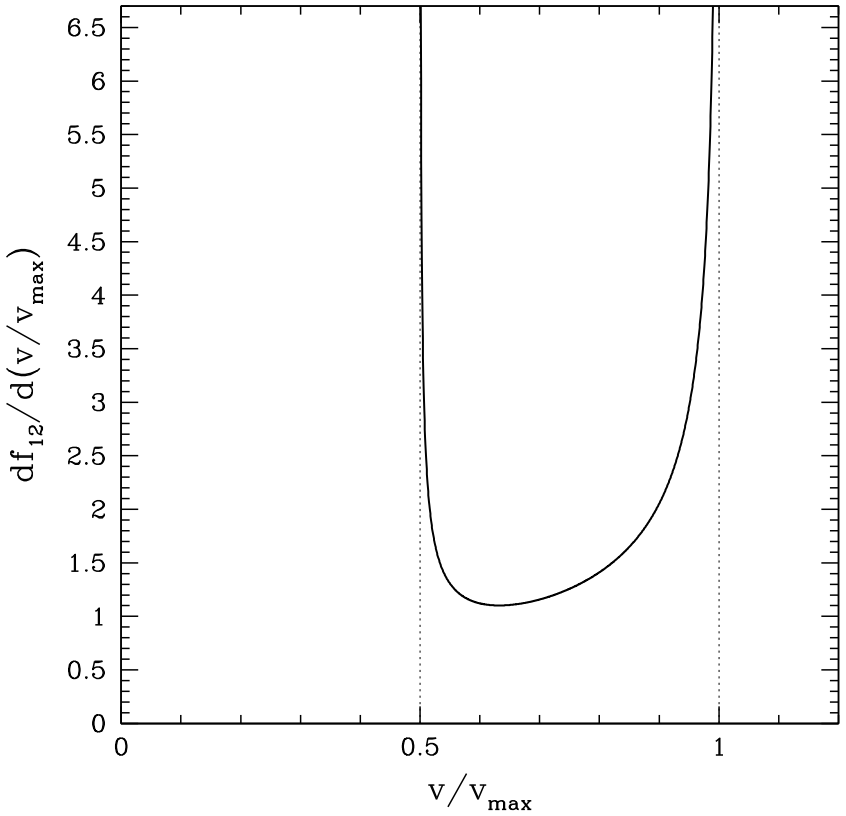

Figure 6. Distribution of the relative approach velocity v_{12} of colliding planetesimals given by Equation (62). The relative velocity is normalized by its maximum value $v_{\max} = e_{12} n_p r$, where e_{12} is the relative eccentricity of the two planetesimals, which is a function of their sizes, see Sections 9.1–9.3. The minimum approach velocity is $v_{\max}/2$.

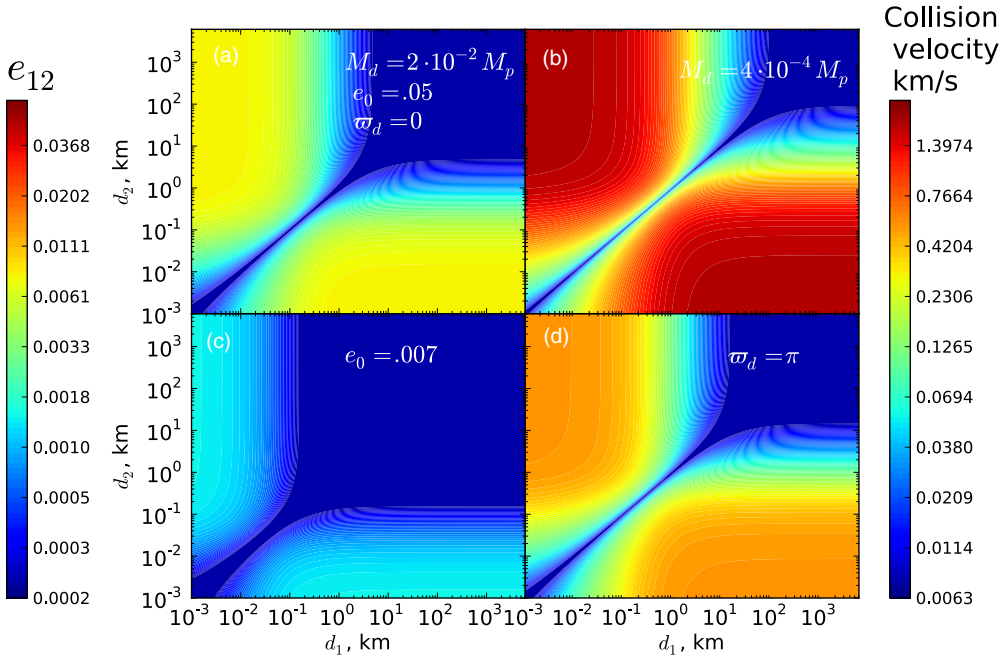

Figure 7. Relative approach velocity (right color bar) and relative eccentricity (left color bar) of planetesimals with sizes d_1 and d_2 experiencing close approach. The calculation is done for the γ Cephei system at 2 AU assuming an eccentric disk with $p = 1$, $q = -1$ and other disk parameters— M_d, e_0, ϖ_d—varying as indicated on the panels. Eccentricity and planetesimal size scales e_c and d_c in different panels can be inferred from Figures 4(a) and (b) and 5(a) and (b).

regimes—strong or weak—we will consider several possibilities separately.

9.1. Strong–Strong Encounters

When both planetesimals are in the strong drag regime, $d_1, d_2 \ll d_c$, both $|A\tau_{d,1}| \ll 1$ and $|A\tau_{d,2}| \ll 1$. Then Equation (64) predicts that

$$e_{12}^{\rm ss} \approx e_c \left| |A\tau_{d,1}| - |A\tau_{d,2}| \right| \tag{65}$$

$$\approx e_c \left| \left(\frac{d_1}{d_c}\right)^{1/2} - \left(\frac{d_2}{d_c}\right)^{1/2} \right|, \tag{66}$$

where we used Equation (34) to express $|A\tau_d|$ in terms of planetesimal sizes. Since $d_{1,2} \ll d_c$ in the strong drag limit, one finds that $e_r^{\rm ss} \lesssim e_c$, which explains the low values of e_r in the lower left corner in the maps in Figure 7.

Physically, in this regime, the relative velocity of two planetesimals is considerably lower than their individual velocities because of the apsidal alignment of their orbits by gas drag, see Marzari & Scholl 2000) and similar magnitudes of $\mathbf{e}_p$.

9.2. Weak–Weak Encounters

When both planetesimals are in the weak drag regime $|A\tau_{d,1}| \gg 1$ and $|A\tau_{d,2}| \gg 1$, one finds using Equation (64) that

$$e_{12}^{\rm ww} \approx e_c \left| |A\tau_{d,1}|^{-1} - |A\tau_{d,2}|^{-1} \right| \tag{67}$$

$$\approx e_c \left| \frac{d_c}{d_1} - \frac{d_c}{d_2} \right|, \tag{68}$$

where Equation (38) has been used. Since $d_{1,2} \gg d_c$ in the weak drag limit, one again finds that $e_r^{\rm ww} \lesssim e_c$, explaining the low relative eccentricity in the upper right corner in the maps in Figure 7.

In this case, apsidal alignment is again at work, lowering e_r compared to $e_p(d_1), e_p(d_2)$. However, now it is caused by the disk+binary gravity, which affects planetesimals in the same way when they are weakly coupled to gas. This is because the gas damps the free eccentricity, but is not strong enough to significantly change the forced eccentricity.

9.3. Weak–Strong Encounters

When one of the planetesimals (e.g., of size d_1) is in the strong drag regime, $|A\tau_{d,1}| \ll 1$, while the other is in the weak drag regime, $|A\tau_{d,2}| \gg 1$, Equation (64) shows that their relative eccentricity e_{12} is just

$$e_{12}^{\rm sw} \approx e_c. \tag{69}$$

One can see that e_{12} is roughly independent of the sizes of particles participating in an encounter.

9.4. Overall e_{12} Scale as a Function of Disk Parameters

The overall scale of e_{12} in each of the maps shown in Figure 7 is characterized by e_{12} in one of the high-velocity corners. According to Section 9.3, this scale is just e_c, which allows us to use the results of Section 7 to understand how the typical e_{12} varies as we change the disk parameters.

A comparison of panels (a) and (b) of Figure 7 shows that disk mass M_d plays an important role in setting $e_{1,2}$: planetesimals in low-mass disks ($M_d = 4 \times 10^{-4}\, M_\odot$) collide with much higher speeds than in higher mass ($M_d = 2 \times 10^{-2}\, M_\odot$) disk. This is because for the chosen value of $e_0 = 0.05$ the low-mass disk is in the BB regime and the value of $e_c \approx 0.05$ is high; see Figure 4(a). Increasing M_d as in panel (a) brings the disk into the DD regime and also close to the valley of stability. For that reason, in a higher mass disk with $M_d = 0.02\, M_\odot$, one gets a much lower $e_c \approx 0.008$.

Lowering e_0 for a high-mass disk as in panel (c) reduces the relative velocity scale even more simply because for $e_0 = 0.007$ the system gets even deeper into the valley of stability, where the corresponding $e_c \approx 1.5 \times 10^{-3}$; see Figure 4(a).

A comparison of panels (a) and (d) shows that changing disk orientation also strongly affects e_r: there is no valley of stability in the misaligned disk and the characteristic eccentricity scale becomes $e_c \approx 0.014$. As a result, particles in a misaligned disk collide at higher speeds than in the aligned disk.

10. DISCUSSION

Our work extends and complements existing results on planetesimal dynamics in binaries in several important ways.

First, for the first time, our solutions for $\mathbf{e}_p$ in Section 5 simultaneously account for a number of key physical ingredients needed for a complete description of the secular dynamics of planetesimals in binaries: the gravity of both the eccentric disk and the eccentric companion as well as the gas drag, which causes orbital phasing of planetesimals and reduces their relative eccentricity in certain regimes.

Second, we provide a rigorous derivation of the equations of eccentricity evolution due to gas drag (15)–(18) in an eccentric disk. Previously, Adachi et al. (1976) derived analogous equations for the case of a circular disk, while Beaugé et al. (2010) proposed a set of empirical equations similar to Equations (15) and (16) but without proper calculation of the constant pre-factors.

Third, we derive an analytic expression (62) for the relative velocity distribution function df_{12}/dv_{12} for locally homogeneous populations of objects with fixed eccentricity vectors, which is appropriate in the limit $|\mathbf{e}_p| \ll 1$ in the presence of gas drag. We also provide an in-depth analysis of e_{12} behavior for objects of different sizes in systems with different parameters (Section 9). Previously the distribution of planetesimal encounter velocities has been explored only numerically by following a large number of trace particles in simulations of different kinds (Thébault et al. 2006, 2008, 2009; Paardekooper et al. 2008; Fragner et al. 2011). Thus, our derivation of df_{12}/dv_r represents an important analytical step in understanding planetesimal dynamics.

We now provide a more detailed comparison of our results with previous studies and discuss the limitations of this work.

10.1. Comparison of Different Dynamical Approximations

The main novelty of our study is the extension of the line of analytical investigation of disk gravity effects, which was started in R13 and SR15 for axisymmetric and non-axisymmetric disks, respectively, by including gas drag. Previous (semi-)analytical studies of planetesimal dynamics in binaries neglected the gravitational effect of the disk.

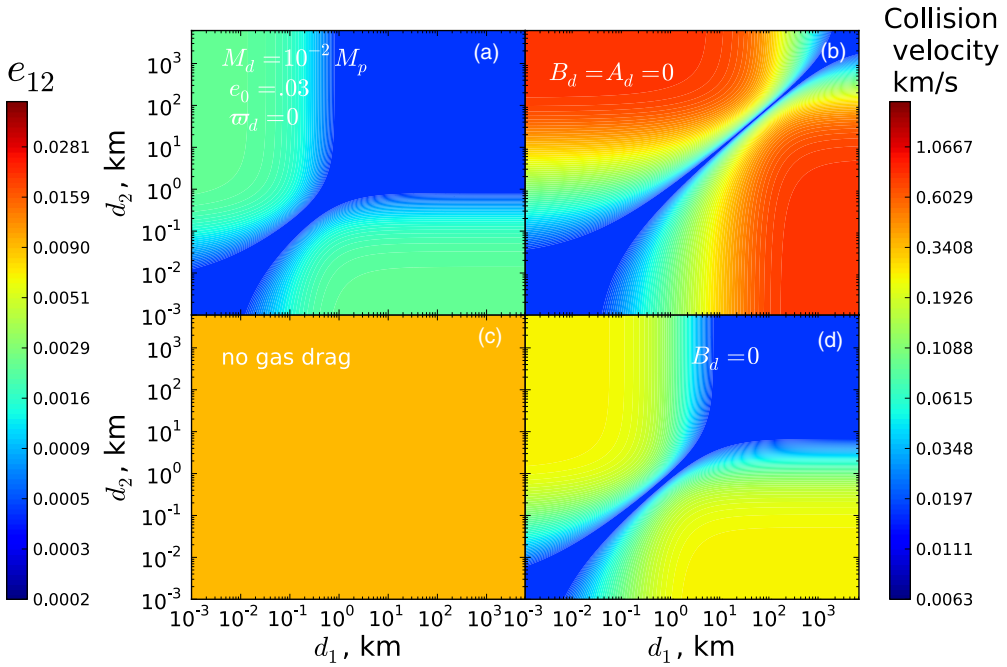

Figure 8. Comparison of different approximations for describing planetesimal dynamics (indicated on panels), as reflected in the map of the relative eccentricity of planetesimals e_r of different sizes; see the text for details. Maps are drawn for an aligned disk in γ Cep at 1 AU (note the different semi-major axis compared to other figures).

Table 1
Different Approximations for Planetesimal Dynamics in Binaries

Gravitational Effects Included	W/O Gas Drag	With Gas Drag
Binary companion only	2, 3	4, 5, 6, 8, 9, 10
Axisymmetric disk and binary companion	7	1
Non-axisymmetric disk and binary companion	8	1

Notes. (1) This work; (2) Giuppone et al. 2011; (3) Heppenheimer 1978; (4) Marzari & Scholl 2000; (5) Paardekooper et al. 2008; (6) Beaugé et al. 2010; (7) Rafikov 2013; (8) Silsbee & Rafikov 2015; (9) Thébault et al. 2006; (10) Xie & Zhou 2008.

Our calculations account for both the precession of planetesimal orbits due to the axisymmetric part of the disk potential and the eccentricity excitation due to its non-axisymmetric component. Disk non-axisymmetry is modeled via its nonzero eccentricity, i.e., $m = 1$ distortion, which can be a function of radius. We expect this approximation to capture the key effect of the disk asymmetry, as higher-m distortions of the disk shape are relatively small (Marzari et al. 2012).

In Table 1 we summarize some existing (semi-)analytical treatments of planetesimal dynamics including this work (note that this list is not exhaustive), classified according to the physical ingredients that are taken into account. We primarily focus on studies of secular effects to put our work in proper context. Our current results cover all dynamical regimes listed in this table in appropriate limits. The majority of previous studies considered planetesimal dynamics in the presence of gas drag with only the direct binary gravitational perturbations taken into account (Marzari & Scholl 2000; Thébault et al. 2004, 2006, 2008, 2009; Paardekooper et al. 2008). As shown in SR15, this approximation is unwarranted as long as the disk mass $M_d \gtrsim 10^{-2}\, M_\odot$ since then the disk potential dominates gravitational perturbation.

We also provide full analytical solutions for test particle dynamics in a general precessing or non-precessing disk without companion perturbation; see Equations (44)–(47). Previously, Beaugé et al. (2010) studied this regime for a precessing disk but did not account for the gravitational effect of the disk (i.e., only gas drag was taken into account). In Figure 8 we illustrate the differences in various descriptions of planetesimal dynamics. It shows the relative eccentricity as a function of planetesimal sizes d_1 and d_2 at 1 AU in an aligned disk of $M_d = 10^{-2} M_p$ and $e_0 = 0.1$ around a primary of γ Cephei in four different limits. Panel (a) presents a full calculation with all physical ingredients (gas drag, gravity of both the eccentric disk and the binary companion) accounted for using the solutions obtained in Section 5.

In panel (b) we show how things change if disk gravity is completely switched off by setting $A_d = B_d = 0$—an approximation common to a number of previous studies (Marzari & Scholl 2000; Thébault et al. 2004, 2006, 2008, 2009; Paardekooper et al. 2008; Beaugé et al. 2010; Leiva et al. 2013). One can see that without disk gravity, relative planetesimal velocities go up by a factor of several. Moreover, the "waist" between the two high-e_{12} regions in panel (b) is narrowest at $d_1 \sim d_2 \sim 10^2$ km, which is considerably larger than in panel (a) where this happens for $d \sim 0.3$ km objects. This difference is in complete agreement with Equations (55) and (56).

In panel (c) we account for the gravitational effect of a non-axisymmetric disk but neglect gas drag ($\tau_d \to \infty$), i.e., use Equations (19)–(21), as was done in SR15. In the absence of gas drag there is no apsidal alignment of planetesimal orbits and they approach each other at random phases. Also, e_r is independent of d_1 and d_2 (the size-dependent drag is absent) explaining uniform color in Figure 8(c). The absence of gas drag results in rather high relative velocities of planetesimals, making their survival in collisions problematic. Thus, apsidal

alignment of planetesimal orbits and eccentricity suppression due to gas drag are very important for the proper description of their dynamics.

Finally, in panel (d) we retain only the axisymmetric component of the disk potential, neglecting the eccentricity excitation by the disk, i.e., $B_d = 0$ but $A_d \neq 0$. In this limit, also neglecting gas drag (accounted for here), R13 predicted a dramatic lowering of $\mathbf{e}_p$. A comparison with panel (a) clearly shows this is not the case when gas drag is included, which can be understood by noting that e_c in Equation (29) can significantly deviate from $|\mathbf{e}_p^{\rm n/drag}|$ because of the $\mathbf{e}_g$ contribution. This is why lowering $|\mathbf{e}_p^{\rm n/drag}|$ by setting $B_d = 0$ and increasing $|A|$ does not necessarily result in smaller e_c, as expected in R13.

To summarize, simultaneously accounting for all the physical processes affecting planetesimals—gas drag, disk, and secondary gravity—is very important for understanding planetesimal growth. Omission of even a single physical ingredient can significantly affect the conclusions drawn from the dynamical calculations.

Previously, Kley & Nelson (2007) and Fragner et al. (2011) numerically explored planetesimal dynamics in gaseous disks that were evolved using direct hydrodynamical simulations. They accounted for the effect of disk gravity on planetesimal motion and at least some of their calculations assumed coplanarity of the disk and the binary. However, even though the setup of these studies is very similar to that of our present work, some subtle differences prevent direct comparison of their results. In particular, when estimating the relative velocities of planetesimals based on their orbit crossing, Kley & Nelson (2007) do not take into account the apsidal phasing of their orbits (Marzari & Scholl 2000), clearly obvious in their Figure 10. As a result they find very high relative speeds even between equal-size planetesimals, which we believe is an artifact of their neglect of apsidal phasing. Fragner et al. (2011) study the case of a circular binary in which apsidal phasing is naturally absent, resulting in high relative speeds of planetesimals. As a result, the applicability of calculations using circular binaries to understanding planetesimal dynamics in eccentric systems like γ Cep is not obvious.

10.2. Limitations of this Work

Finally, we discuss the limitations of our study. Some of them have to do with the adoption of secular, i.e., orbit-averaged, approximation. While averaging over the planetesimal orbit is justified because n_p^{-1} is always much shorter than other periodicities (e.g., of planetesimal apsidal precession), when averaging over the longer binary period, one may overlook important dynamical features of the systems possessing very massive disks. Indeed, Equation (6) suggests that for $M_d \sim 0.1\,M_\odot$, the planetesimal precession rate $|A_d|$ becomes comparable to the binary angular frequency—$n_p \approx 0.1$ yr^{-1} for γ Cephei. In these conditions, averaging over the latter is not justified and new effects, such as the possibility of evection resonance (Touma & Wisdom 1998) inside the disk, may also affect planetesimal dynamics.

Other effects omitted in our study, such as the density waves or higher-m contributions to the azimuthal mass distribution in the disk and short-term fluctuations of the disk potential, may also affect planetesimal dynamics. They may account for some of the difference between the results of this work, which uses a secular, time-averaged description of the disk and binary potential, and direct numerical studies of Kley & Nelson (2007) and Fragner et al. (2011). Planetesimal eccentricity can be additionally excited by the stochastic gravitational perturbations due to the turbulence in the disk. This issue has been previously investigated for disks around single stars (Ida et al. 2008; Yang et al. 2009, 2012) and for circumbinary disks (Meschiari 2012).

Coplanarity of the disk and the binary orbit is another restriction that can be easily eliminated in future studies. We believe that small but non-zero inclination (Xie & Zhou 2009) would not affect our solutions for the behavior of planetesimal eccentricity. However, as shown in Xie et al. (2010), such non-zero inclination has a strong effect on planetesimal collision rates.

There is also room for improvement within the framework of our model. Some approximations that we adopt, such as the power-law behavior of $\Sigma(a)$ and $e_d(a)$ and constant[2] $\varpi_d(a)$, are dictated by our desire to obtain analytical solutions using the results of SR15 whenever possible. Also, we did not investigate the conditions under which our model (1) represents a steady-state solution for a fluid disk perturbed by a companion (Statler 2001). More refined semi-analytical or numerical calculations using improved disk models are certainly desirable but are unlikely to seriously affect our results and conclusions.

11. SUMMARY

We studied secular dynamics of planetesimals and explored prospects for planet formation around one of the components of an eccentric binary. We believe that our study includes most, if not all, of the important physical ingredients relevant for this problem—perturbations due to the binary, gas drag, and gravitational effects of an eccentric disk. This is the first time planetesimal dynamics in binaries have been studied analytically in such generality. The analytical nature of our solutions for planetesimal dynamical variables allowed us to explore their dependence on system parameters in great detail.

Our main results can be summarized as follows.

1. We find that under the action of gas drag as well as the gravitational effects of the binary companion *and the eccentric disk*, the planetesimal eccentricity vector $\mathbf{e}_p$ converges to a constant value depending on the planetesimal size and the disk and binary properties. We obtained complete analytical solutions for $\mathbf{e}_p$ in the case of a non-precessing disk and analyzed them in detail, extending the results of previous studies.
2. We showed that relative particle–gas (Equation (33)) and particle–particle velocities can be expressed as simple functions of only two key parameters—the characteristic eccentricity e_c and planetesimal size d/d_c in units of characteristic size d_c, given by Equations (29) and (31). The behavior of these variables has been explored in detail in Section 7.
3. We show that in massive disks containing enough gas to form giant planets ($M_d \gtrsim 10^{-2}\,M_\odot$), planetesimal dynamics are always in the regime where the apsidal precession of planetesimal orbits is dominated by disk gravity, i.e., in the DB or DD regimes in the classification of SR15. Significantly eccentric ($e_0 \gtrsim 10^{-3}$) disks also dominate the eccentricity excitation of planetesimals by their gravity (DD regime). This emphasizes the key role of the disk gravity in relation to planet formation in binaries.

[2] Variable $\varpi_d(a)$ can be used to describe disks with density waves.

4. We derive the explicit form of the relative velocity distribution between the populations of planetesimals with different sizes and show that it depends only on the relative eccentricity e_{12} of the approaching objects.
5. In disks aligned with the binary, planetesimals collide with lower velocities than in misaligned disks. Thus, planetesimal growth favors disk–binary apsidal alignment.
6. We also present analytical results for the dynamics of planetesimals in precessing disks in certain limits.

Our results will be used in Paper II to understand planet formation in small separation binaries, such as γ Cep and α Cen. They can also be used to understand the circumbinary planet formation.

We are grateful to Jihad Touma for useful discussions.

APPENDIX A

LOCAL APPROXIMATION

Here we review local (or guiding center) approximation, which is often used in studies of planetesimal and galactic dynamics (Binney & Tremaine 2008) and forms the basis of the so-called Hill approximation (Hénon & Petit 1986; Hasegawa & Nakazawa 1990). In this approach, eccentric motion of a planetesimal is considered in a locally Cartesian frame (x_p, y_p), with $\mathbf{e}_x$, $\mathbf{e}_y$ pointing in the radial and horizontal directions, correspondingly. The origin of this frame is in circular Keplerian motion at some characteristic semi-major axis a_0, which is close to the planetesimal semi-major axis a_p, so that $b_p \equiv |a_p - a_0| \ll a_p$. Equations of motion for a particle of mass m_p subject to external force $\mathbf{F} = (F_x, F_y)$ can be reduced to

$$\ddot{x}_p - 2n_p\dot{y}_p - 3n_p^2 x_p = F_x/m_p, \quad \ddot{y}_p + 2n_p\dot{x}_p = F_y/m_p. \tag{A1}$$

Provided that $e_p \ll 1$, one can represent planetesimal motion unperturbed by external forces as

$$x_p = b_p - a_0(k_p \cos n_p t + h_p \sin n_p t),$$
$$y_p = \psi_p - \frac{3}{2}n_p b_p t + 2a_0(k_p \sin n_p t - h_p \cos n_p t), \tag{A2}$$

where ψ_p is a constant and $\mathbf{e}_p = (k_p, h_p)$. This is an exact solution of Equations (A1) with $\mathbf{F} = 0$ and is a superposition of linear shear and epicyclic motion.

Assuming that fluid in a gaseous disk also moves on eccentric Keplerian orbits, motion of the gas can be represented by analogous equations

$$x_g = b_g - a_0(k_g \cos n_p t + h_g \sin n_p t),$$
$$y_g = \psi_g - \frac{3}{2}n_p b_g t + 2a_0(k_g \sin n_p t - h_g \cos n_p t). \tag{A3}$$

Relative motion of a particular fluid element and a particle is described using relative coordinates $x_r = x_p - x_g$, $y_r = y_p - y_g$. According to Equations (A2)

$$x_r = b_r - a_p(k_r \cos n_p t + h_r \sin n_p t),$$
$$y_r = \psi_r - \frac{3}{2}n_p b_r t + 2a_p(k_r \sin n_p t - h_r \cos n_p t), \tag{A4}$$

where $k_r \equiv k_p - k_g$, $h_r \equiv h_p - h_g$ are the components of the relative eccentricity vector, $b_r \equiv b_p - b_g$ is the semi-major axis separation between the particle and fluid element, and $\psi_r \equiv \psi_p - \psi_g$. We have also used the fact that $a_g \approx a_0 \approx a_p$ and switched from a_0 to a_p.

Velocity of Keplerian motion in the local approximation is obtained by differentiating Equations (A4) with respect to time. In particular, relative particle–gas velocity is given by

$$v_{x,r} = n_p a_p(k_r \sin n_p t - h_r \cos n_p t),$$
$$v_{y,r} = -\frac{3}{2}n_p b_r + 2n_p a_p(k_r \cos n_p t + h_r \sin n_p t). \tag{A5}$$

Analogous formulae apply to the relative motion of two planetesimals with sizes d_1 and d_2, with the replacement $e_r \to e_{12}$, $b_r \to b_{12}$, $(x_r, y_r) \to (x_{12}, y_{12})$, and so on. In particular, Equations (A4) shows that two objects with $|b_{12}| < a_p e_{12}$ can experience close approaches. When this happens, $x_{12} = y_{12} = 0$ and b_{12} can be eliminated from Equations (A5) giving

$$v_{12,y}(x_{12} = 0) = \frac{1}{2}n_p a_p(k_{12} \cos n_p t + h_{12} \sin n_p t), \tag{A6}$$

(here $\mathbf{e}_{12} = (k_{12}, h_{12})$) so that the relative approach velocity (i.e., the velocity unaffected by the mutual gravitational attraction of particles) is

$$v_{12} = n_p a_p \left[k_{12}^2 + h_{12}^2 - (3/4)(k_{12} \cos n_p t + h_{12} \sin n_p t)^2\right]^{1/2}. \tag{A7}$$

Whenever a particle is affected by forces other than the stellar gravity, i.e., $\mathbf{F} \neq 0$, solutions (A2) are no longer strictly valid. However, one can still represent particle motion via these solutions, assuming that orbital elements osculate, i.e., evolve, in time. Hasegawa & Nakazawa (1990) derived equations for the orbital element evolution, in particular

$$\dot{a}_p = \dot{b}_p = \frac{2F_y}{n_p m_p}, \quad \dot{k}_p = \frac{1}{n_p a_p m_p}(2F_y \cos n_p t + F_x \sin n_p t),$$
$$\dot{h}_p = \frac{1}{n_p a_p m_p}(2F_y \sin n_p t - F_x \cos n_p t). \tag{A8}$$

For a given force expression $\mathbf{F}$, these equations, after averaging over the orbital period, represent the extra terms entering the Equations (3) and (4).

APPENDIX B

PLANETESIMAL ECCENTRICITY IN A PRECESSING DISK IN THE CASE OF LINEAR DRAG

Here we derive the full time-dependent solution for planetesimal eccentricity starting with arbitrary initial conditions and assuming that the gas drag is linear, i.e., τ_d in Equation (17) is a constant independent of $\mathbf{e}_p$. We also include a possibility of uniform disk precession so that $\varpi_d(t) = \dot{\varpi}_d t + \varpi_{d0}$. Then Equations (3) and (4) represent a linear system of equations which can be trivially solved to give

$$\begin{Bmatrix} k(t) \\ h(t) \end{Bmatrix} = e_{\rm free} e^{-t/\tau_d} \begin{Bmatrix} \cos(At + \varpi_0) \\ \sin(At + \varpi_0) \end{Bmatrix} + \begin{Bmatrix} k_{\rm f} \\ h_{\rm f} \end{Bmatrix}, \tag{B1}$$

where the first term represents the free eccentricity, with $e_{\rm free}$ and ϖ_0 being constant, while the second is the forced eccentricity

$\mathbf{e}_f = (k_f, h_f) = \mathbf{e}_{f,b} + \mathbf{e}_{f,d}$, where $\mathbf{e}_{f,b}$ is given by Equation (25) and

$$\mathbf{e}_{f,d} = \left[\frac{e_g^2 + \tau_d^2 B_d^2}{1 + \tau_d^2 (A - \dot{\varpi}_d)^2}\right]^{1/2} \left\{ \begin{array}{c} \cos(\varpi_d(t) + \phi) \\ \sin(\varpi_d(t) + \phi) \end{array} \right\},$$
$$\cos\phi = \frac{e_g - \tau_d^2 B_d (A - \dot{\varpi}_d)}{\left(e_g^2 + \tau_d^2 B_d^2\right)^{1/2} \left[1 + \tau_d^2 (A - \dot{\varpi}_d)^2\right]^{1/2}}. \quad \text{(B2)}$$

In the limit of slow precession $|\dot{\varpi}_d| \ll |A|$ one finds that $\mathbf{e}_f$ is given by expressions (24)–(27). Generally, the relative planetesimal–gas eccentricity $\mathbf{e}_r = \mathbf{e}_f - \mathbf{e}_g$ is

$$\mathbf{e}_r = \mathbf{e}_{f,b} - \tau_d \frac{B_d + e_g (A - \dot{\varpi}_d)}{\left[1 + \tau_d^2 (A - \dot{\varpi}_d)^2\right]^{1/2}} \left\{ \begin{array}{c} \cos(\varpi_d(t) - \phi_r) \\ \sin(\varpi_d(t) - \phi_r) \end{array} \right\},$$
$$\cos\phi_r = \frac{\tau_d (A - \dot{\varpi}_d)}{\left[1 + \tau_d^2 (A - \dot{\varpi}_d)^2\right]^{1/2}}. \quad \text{(B3)}$$

The first forced term $\mathbf{e}_{f,b}$ results from excitation by the binary companion. It is constant in time and is independent of $\dot{\varpi}_d$. The second term is induced by the disk via both its gravitational potential and gas drag. This contribution to $\mathbf{e}_f$ circulates at the disk precession frequency $\dot{\varpi}_d$ and its amplitude is sensitive to $\dot{\varpi}_d$.

Independent of the initial conditions (i.e., the values of $e_{\rm free}$ and ϖ_0), the free eccentricity contribution damps out on a characteristic timescale τ_d. As a result, in the long run, $\mathbf{e}_p$ inevitably converges to $\mathbf{e}_f$.

In the limit of strong gas drag, $\tau_d \to 0$, one finds that $\mathbf{e}_f \to \mathbf{e}_g$ as expected, since drag is strong enough to align planetesimal orbits with fluid trajectories. In this limit, the relative eccentricity between planetesimals of different sizes having different damping times $\tau_{d,1}$ and $\tau_{d,2}$ is

$$e_{12} \to |A - \dot{\varpi}_d||\tau_{d,1} - \tau_{d,2}| \left[\left(e_c^{\rm pr} \sin\varpi_d\right)^2 + \left(e_c^{\rm pr} \cos\varpi_d + k_b \frac{A}{A - \dot{\varpi}_d}\right)^2 \right]^{1/2}, \quad \tau_{d,1}, \tau_{d,2} \ll |A - \dot{\varpi}_d|^{-1}, \quad \text{(B4)}$$

where $e_c^{\rm pr}$ is given by Equation (45).

In the opposite extreme, $\tau_d \to \infty$ (weak drag), one finds $\phi \to \pi$ and $\mathbf{e}_f$ reduces to the forced eccentricity value (with disk precession) obtained in SR15. The relative velocity becomes

$$e_{12} \to \frac{1}{|A - \dot{\varpi}_d|} \left|\tau_{d,1}^{-1} - \tau_{d,2}^{-1}\right| \left[\left(e_c^{\rm pr} \sin\varpi_d\right)^2 + \left(e_c^{\rm pr} \cos\varpi_d + k_b \frac{A - \dot{\varpi}_d}{A}\right)^2 \right]^{1/2}, \quad \tau_{d,1}, \tau_{d,2} \gg |A - \dot{\varpi}_d|^{-1}. \quad \text{(B5)}$$

Note that in this expression, k_b is multiplied by a factor different from that in Equation (B4). However, it is clear that in both limiting cases, $e_{12} \ll e_1, e_2$, i.e., the relative planetesimal eccentricity is much less than the individual eccentricities e_1 and e_2, a result that remains valid in a precessing disk.

APPENDIX C

PLANETESIMAL ECCENTRICITY IN A PRECESSING DISK IN THE CASE OF QUADRATIC DRAG

In the case of quadratic drag (10), Figure 2(b) clearly shows the phenomenon of $\mathbf{e}_p$ convergence to a quasi-stationary limit cycle behavior, similar to the results of Appendix B. This behavior is further illustrated in Figure 9, where we show the dependence of the limit cycles on planetesimal size d_p and disk precession rate $\dot{\varpi}_d$. Because of the nonlinear drag law, the shapes of the limit cycles in general deviate from ellipses.

Nevertheless, their gross features still can be understood in our linear solution (B3). In particular, limit cycles are not centered on $(k_r, h_r) = 0$ because of the binary companion perturbations, i.e., non-zero $\mathbf{e}_{f,b}$ varying as d_p (and τ_d) change. The amplitude of the limit cycles goes down for smaller d_p because τ_d is also smaller, which, according to Equation (B3), reduces the oscillating contribution to $\mathbf{e}_r$. As we vary $\dot{\varpi}_d$ in Figure 9(b), the binary contribution stays unchanged and all limit cycles stay centered on the same point in h_r-k_r space.

Their sizes vary with $\dot{\varpi}_d$ as predicted by Equation (B3). They shrink at high $|\dot{\varpi}_d| \sim |A|$, in agreement with Equation (B3). For slow precession, $|\dot{\varpi}_d| \ll |A|$ limit cycles converge to the trajectory for the non-precessing disk solution (24) in which ϖ_d is set to vary as $\varpi_d(t) = \dot{\varpi}_d t + \varpi_{d0}$. Note that such a convergence to solution (24) is obvious only in the case of $|\dot{\varpi}_d \tau_d| \ll 1$, i.e., when gas drag allows $\mathbf{e}_p$ to quickly re-adjust to a new "quasi-static" solution as ϖ_d changes. This is the case shown in Figure 9(b). In the opposite case of $|\dot{\varpi}_d \tau_d| \gg 1$ (and $|\dot{\varpi}_d| \ll |A|$), this convergence is not obvious as the disk precession constantly drives free eccentricity, while the gas drag is not strong enough to quickly damp it. We leave detailed exploration of such topics to a future study.

Now, let us rewrite Equations (3) and (4) in terms of the relative particle–gas eccentricity components k_r and h_r:

$$\frac{dh_r}{dt} = Ak_r - \frac{h_r}{\tau_d} + B_b + [(A - \dot{\varpi}_d) e_g + B_d] \cos\varpi_d(t), \quad \text{(C1)}$$

$$\frac{dk_r}{dt} = -Ah_r - \frac{k_r}{\tau_d} - [(A - \dot{\varpi}_d) e_g + B_d] \sin\varpi_d(t), \quad \text{(C2)}$$

with τ_d given by Equation (18) and dependent upon e_r.

The explicit time dependence of the last terms in these nonlinear equations precludes us from finding their general analytical solutions even in the case of the limit-cycle behavior. However, we can still obtain analytical results for planetesimal eccentricity in the two limiting cases, reviewed next.

First, one can assume that the binary companion dominates eccentricity forcing, which implies that the condition (42) is fulfilled. Then one can drop the last ϖ_d-dependent terms in Equations (C1) and (C2), removing the explicit time dependence from them. This is essentially equivalent to neglecting both the gravitational effect of the disk, i.e., $|\mathbf{e}_d| \to 0$, and the gas eccentricity, e_g, compared to $|\mathbf{e}_b|$. As a result, we find a steady-state solution (43) for $k_r \approx k_p$ and $h_r \approx h_p$, which is essentially the Equations (22) and (23) with $|\mathbf{e}_d|, |\mathbf{e}_g| \to 0$. Then planetesimal dynamics are described by the analytical results of Section 5 with $e_c \approx |B_b/A|$.

In the opposite extreme of weak eccentricity excitation by the binary companion we introduce new coordinates

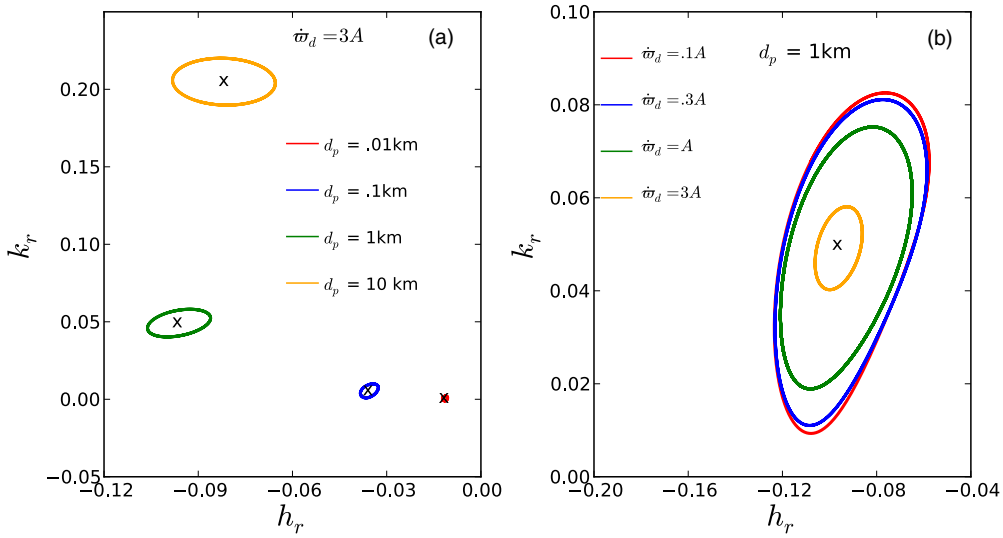

Figure 9. Limit cycles to which the relative gas–planetesimal eccentricity vector $\mathbf{e}_r$ converges in precessing disks. Panel (a) shows evolution of the limit cycles as a function of planetesimal size d_p, while in panel (b) we vary the disk precession rate $\dot{\varpi}_d$. Calculations have been performed at $a_p = 2.5$ AU in a standard aligned disk with $M_d = 10^{-3} M_p$, $e_0 = 0.04$, $a_{\rm out} = 5$ AU in γ Cep system. These parameters place planetesimal dynamics in the strong binary perturbation regime; see Section 6.1. Crosses mark the centers of the limit cycles computed according to Equation (43). Note the evolution of the positions and shapes of the limit cycles as d_p and $\dot{\varpi}_d$ are varied.

$H \equiv k_g h_r - h_g k_r$, $K \equiv h_g h_r + k_g k_r$ (see Beaugé et al. 2010 for a similar treatment). Then the evolution of H and K is given by

$$\frac{dH}{dt} = (A - \dot{\varpi}_d)\, K - \frac{H}{\tau_d} + B_b k_g(t) + e_g \left[(A - \dot{\varpi}_d)\, e_g + B_d \right], \tag{C3}$$

$$\frac{dK}{dt} = -(A - \dot{\varpi}_d)\, H - \frac{K}{\tau_d} + B_b h_g(t). \tag{C4}$$

When the eccentricity excitation by the companion is small, we can drop the B_b terms in these equations, removing the explicit time-dependence, which appears because of circulating k_g and h_g. As a result, we find the steady state solutions for H and K in the implicit form

$$K = e_c^{\rm pr} e_g \frac{(A - \dot{\varpi}_d)^2\, \tau_d^2}{1 + (A - \dot{\varpi}_d)^2\, \tau_d^2}, \quad H = -e_c^{\rm pr} e_g \frac{(A - \dot{\varpi}_d)\, \tau_d}{1 + (A - \dot{\varpi}_d)^2\, \tau_d^2}, \tag{C5}$$

where τ_d is a function of the relative particle–gas eccentricity $e_r = e_g^{-1}(K^2 + H^2)^{1/2}$ given by Equation (44). This solution corresponds to the eccentricity vector $\mathbf{e}_p$ fixed in a disk frame, which uniformly precesses at the rate $\dot{\varpi}_d$.

Using these solutions, it is trivial to show that $\mathbf{e}_p \to \mathbf{e}_{f,d}$ given by Equation (B2) with B_b set to zero. That in the weak binary perturbation regime we find the same expression for $\mathbf{e}_p$ as in the case of linear drag is not surprising: with $B_b = 0$ one finds that $|\mathbf{e}_r|$ is constant in time, so that τ_d is also constant. Then Equations (C3) and (C4) are the same as in the linear drag case and have the same steady state solutions (C5).

REFERENCES

Adachi, I., Hayashi, C., & Nakazawa, K. 1976, PThPh, 56, 1756
Artymowicz, P., & Lubow, S. H. 1994, ApJ, 421, 651
Barnes, R., & Greenberg, R. 2006, ApJ, 638, 478
Batygin, K., Morbidelli, A., & Tsiganis, K. 2011, A&A, 533, A7
Beaugé, C., Leiva, A. M., Haghighipour, N., & Otto, J. C. 2010, MNRAS, 408, 503
Binney, J., & Tremaine, S. 2008, Galactic Dynamics (Princeton, NJ: Princeton University Press)
Chauvin, G., Beust, H., Lagrange, A.-M., & Eggenberger, A. 2011, A&A, 528, A8
Desidera, S., & Barbieri, M. 2007, A&A, 462, 345
Dumusque, X., Pepe, F., Lovis, C., et al. 2012, Natur, 491, 207
Dvorak, R. 1982, OAWMN, 191, 423
Fragner, M. M., Nelson, R. P., & Kley, W. 2011, A&A, 528, A40
Giuppone, C. A., Leiva, A. M., Correa-Otto, J., & Beaugé, C. 2011, A&A, 530, A103
Harris, R. J., Andrews, S. M., Wilner, D. J., & Kraus, A. L. 2012, ApJ, 751, 115
Hasegawa, M., & Nakazawa, K. 1990, A&A, 227, 619
Hatzes, A. P. 2013, ApJ, 770, 133
Hatzes, A. P., Cochran, W. D., Endl, M., et al. 2003, ApJ, 599, 1383
Hénon, M., & Petit, J.-M. 1986, Celest. Mech. Dynam. Astron., 38, 67
Heppenheimer, T. A. 1978, A&A, 65, 421
Ida, S., Guillot, T., & Morbidelli, A. 2008, ApJ, 686, 1292
Ida, S., Kokubo, E., & Makino, J. 1993, MNRAS, 263, 875
Kley, W., & Nelson, R. 2007, arXiv:0705.3421
Kley, W., & Nelson, R. P. 2008, A&A, 486, 617
Kley, W., Papaloizou, J. C. B., & Ogilvie, G. I. 2008, A&A, 487, 671
Kozai, Y. 1962, AJ, 67, 591
Leiva, A. M., Correa-Otto, J. A., & Beaugé, C. 2013, MNRAS, 436, 3772
Lidov, M. L. 1962, P&SS, 9, 719
Marzari, F., Baruteau, C., Scholl, H., & Thebault, P. 2012, A&A, 539, A98
Marzari, F., & Scholl, H. 2000, ApJ, 543, 328
Marzari, F., Scholl, H., Thébault, P., & Baruteau, C. 2009a, A&A, 508, 1493
Marzari, F., Thébault, P., & Scholl, H. 2009b, A&A, 507, 505
Meschiari, S. 2012, ApJL, 761, L7
Müller, T. W. A., & Kley, W. 2012, A&A, 539, A18
Murray, C. D., & Dermott, S. F. 1999, Solar System Dynamics (Cambridge: Cambridge Univ. Press)
Ogilvie, G. 2001, MNRAS, 325, 231
Okazaki, A. T., Bate, M. R., Ogilvie, G. I., & Pringle, J. E. 2002, MNRAS, 337, 967
Paardekooper, S.-J., Thébault, P., & Mellema, G. 2008, MNRAS, 386, 973
Picogna, G., & Marzari, F. 2013, A&A, 556, A148
Rafikov, R. R. 2013, ApJL, 765, L8
Rafikov, R. R., & Silsbee, K. 2015, ApJ, 798, 70
Regály, Zs., Sándor, Zs., Dullemond, C. P., & Kiss, L. L. 2011, A&A, 528, A93
Silsbee, K., & Rafikov, R. R. 2015, ApJ, 798, 71
Statler, T. S. 2001, AJ, 122, 2257
Thébault, P. 2011, CeMDA, 111, 29

Thébault, P., Marzari, F., & Scholl, H. 2006, Icar, 183, 193
Thébault, P., Marzari, F., & Scholl, H. 2008, MNRAS, 388, 1528
Thébault, P., Marzari, F., & Scholl, H. 2009, MNRAS, 393, L21
Thébault, P., Marzari, F., Scholl, H., Turrini, D., & Barbieri, M. 2004, A&A, 427, 1097
Touma, J., & Wisdom, J. 1998, AJ, 115, 1653
Veras, D., & Armitage, P. J. 2007, ApJ, 661, 1311
Xie, J.-W., & Zhou, J.-L. 2008, ApJ, 686, 570
Xie, J.-W., & Zhou, J.-L. 2009, ApJ, 698, 2066
Xie, J.-W., Zhou, J.-L., & Ge, J. 2010, ApJ, 708, 1566
Yang, C.-C., Mac Low, M.-M., & Menou, K. 2009, ApJ, 707, 1233
Yang, C.-C., Mac Low, M.-M., & Menou, K. 2012, ApJ, 748, 79
Zhao, G., Xie, J.-W., Zhou, J.-L., & Lin, D. N. C. 2012, ApJ, 749, 172